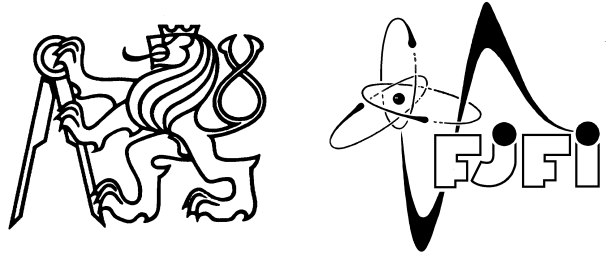


CZECH TECHNICAL UNIVERSITY IN PRAGUE

FACULTY OF NUCLEAR SCIENCES
AND PHYSICAL ENGINEERING

DEPARTMENT OF PHYSICS



**Interpretation of X-Ray Spectra Emitted
from Inhomogenous Plasma**

DIPLOMA THESIS

2011

Michal Šmíd

Zadání.

Declaration

I hereby declare that this diploma thesis is completely my own work and that I used only the cited sources.

Prohlášení

Prohlašuji, že jsem svou diplomovou práci vypracoval samostatně a použil jsem pouze podklady (literaturu, projekty, SW atd.) uvedené v příloženém seznamu.

Nemám závažný důvod proti užití tohoto školního díla ve smyslu §60 Zákona č.121/2000 Sb., o právu autorském, o právech souvisejících s právem autorským a o změně některých zákonů (autorský zákon).

V Praze dne _____

podpis

Acknowledgment

I would like to thank to H. Scott and M. Busquet for providing me the access and support to their codes, and to R. Liska for performing the hydrodynamics simulations.

Název práce:

Interpretace rentgenových spekter emitovaných nehomogenním plazmatem

Autor: Bc. Michal Šmíd

Obor: Fyzika a technika termojaderné fúze

Druh práce: Diplomová práce

Vedoucí práce: Ing. Oldřich Renner, DrSc., FzÚ, AV ČR

Abstrakt:

V této práci představuji nově vyvinutý výpočetní rámec pro postprocessing hydrodynamických dat, který aplikuji na tvorbu syntetických spekter pro simulaci laserem ozářené hliníkové folie. Použité kódy jsou také úspěšně použity na vyhodnocení rentgenových spekter naměřených při dvoufoliových experimentech provedených v laboratoři PALS. Těmito experimenty studujeme interakci laserového plazmatu se stěnou, což je důležité jak pro základní výzkum, tak i vzhledem k aplikacím v různých fúzních zařízeních.

Klíčová slova: rentgenová spektroskopie, laserové plazma, postprocessing hydrodynamických dat, interakce plazma - stěna.

Title:

Interpretation of x-ray spectra emitted from inhomogeneous plasma

Author: Bc. Michal Šmíd

Abstract:

The newly developed computational spectroscopic framework for hydrodynamic data postprocessing is introduced and the spectra from its application at simulation of laser irradiated Al foil are presented along the basic evaluation of measured x-ray spectra from double-foil experiments performed at Prague Asterix Laser System. These experiments are targeted at studying the laser-plasma wall interaction (LPWI) which is of large importance for basic research as well as for its applications in various fusion devices.

Key words: Plasma-wall interaction, Laser-produced plasma, hydrodynamic data postprocessing, x-ray spectroscopy.

Contents

1. Introduction	8
2. Elements of plasma radiation	10
2.1. Line spectrum	10
2.2. Satellite lines	11
2.3. Line shapes	12
3. Double-foil experiments	14
3.1. Vertical-geometry Johann spectrometer	15
4. Theoretical spectra	20
4.1. Collisional-radiative model	20
4.2. Simulation codes	21
4.3. Atomic model	25
4.4. PALE Hydrodynamics	27
4.5. Time-dependent and steady-state regimes	28
4.6. Data flow	32
5. Hydrocode postprocessing	33
5.1. Work overview	33
5.2. Case A: The steady-state on-axis simulation	35
5.3. Case B: The time-dependent on-axis simulation	38
5.4. Case C: Full geometry, no velocity effects	39
5.5. Case D: Full geometry simulation with ion velocities included	40
6. Sample application in experimental spectra evaluation	42
6.1. Methodology	42
6.2. Experimental data	43
6.3. Single-cell evaluation	44

6.4. Results	46
7. Conclusion	48
A. Hullac input files	I
B. Generator files for Cretin	III
C. CompSpect manual	VI
C.1. Introduction	VI
C.2. Application description	VI
C.3. Usage guide	VIII
C.4. Keystroke function reference	X

1. Introduction

The interpretation of x-ray radiation emitted from non-homogeneous plasma is of great importance as a diagnostic tool in studying laser-plasma phenomena. The difficulty of analyzing such spectra lies in the fact that we are not able to evaluate them directly, but a set of simulations need to be processed to get synthetic spectra which can be compared to the measured one.

This radiation is sometimes interpreted using a homogeneous plasma assumption, however, the detailed study of the temporal and spatial variation of x-ray emission presented in this thesis shows the relevance and limits of this approach, and tries to build up more precise interpretation.

This thesis is a part of a long-term project of performing and evaluating laser-plasma wall interaction (LPWI) experiments. The interaction of plasma with solid materials (walls) is of great importance for basic research studying the properties and behavior of hot plasmas, as well as for its possible applications in future fusion devices.

For example, in tokamaks used in *magnetic confinement fusion*, the plasma diffuses despite the magnetic gradient from inwards towards the outer parts of the tokamak. Consequently, it reaches its wall and interacts with it. This one occurrence of plasma-wall interaction is intensively studied.

In the most common scheme of indirectly driven *inertial confinement fusion* we can see another example of plasma-wall interaction: the fusion *pellet* is inserted in the hohlraum whose inner surface is irradiated with laser beams in order produce a plasma which interacts with the pellet.

The *laser-produced plasma* is generated using an intensive laser beam impinging on a solid target, typically a thin foil, where the matter is ionized and a plasma jet perpendicular to the target surface is produced. This represents a very efficient tool for investigating the plasma-wall interactions because the expanding plasma jets with parameters defined by the laser-matter conditions can produce different interaction scenarios.

The largest part of this thesis consists of the detailed spectral postprocessing of existing Prague Arbitrary Lagrangian Eulerian (PALE) code[1] simulations which includes non-

1. Introduction

homogeneous plasma with time evolution. In the final chapter, produced synthetic spectra are compared with the experimental ones to show the possibilities of this approach and prospective enhancements for future development.

The unit *Ångström* ($1 \text{ \AA} = 0.1 \text{ nm}$) is used in this thesis for wavelengths, as it is usual in the field of x-ray spectroscopy.

2. Elements of plasma radiation

Radiation emitted from hot dense plasmas is probably the most important diagnostic tool for these plasmas because it carries information about the local plasma conditions. For short lifetime plasmas, that we focus on in this thesis, x-ray radiation is a very efficient diagnostic tool.[2]

The emission spectrum is produced by electron transitions which can be classified with respect to the initial and the final transition states to *free-free*, *free-bound*, and *bound-bound* transitions. It is obvious that the photons emitted during the first two types of processes contribute to the *continuous spectrum*, while the latter process contributes to the *line spectrum*, which is of our main interest.

In this chapter, only the very basics of plasma physics concerning line radiation are briefly discussed.

2.1. Line spectrum

The *line emission* occurs only in plasmas where ions are not fully stripped. In hot dense plasmas, that we are concerned with, this is true only for the intermediate and high- Z plasmas.

The main process contributing to the line spectrum is the *spontaneous decay* in which an excited ion decays into a lower, usually ground, state emitting a photon with energy corresponding to the difference between the two electron states. The energies of those lines are given by the Bohr formula[?],

$$E = \frac{Z^2 e^3}{2a_0} \left(\frac{1}{n_l^2} - \frac{1}{n_u^2} \right), \quad (2.1)$$

where n_l and n_u are the principal quantum numbers of the lower and the upper state of the transition.

For the hydrogen-like ions (that is ions with only one bound electron left), the lines are organized into *series* according to the final state of the transition. The series are denoted

2. Elements of plasma radiation

series	abbrev.	n_1
Lyman	Ly	1
Balmer	Ba	2
Paschen	Pa	3
Brackett	Br	4
	...	

Table 2.1.: Names of spectroscopic series

by names, as seen in table 2.1. The lines from each series are denoted with a Greek letter in its subscript, e.g. Ly_α refers to $n_1 = 1$ and $n_u = 2$.

2.2. Satellite lines

Satellite lines constitute another part of the line spectrum. They usually appear as low intensity features near strong *parent* lines. They are caused by the decay of double- or multiply-excited ions.

If one of the excited electrons of a multiply-excited ion decays into a lower state, it emits a photon with energy close to that emitted from the same transition in a single-excited ion. The presence of another excited electron, so called *spectator*, slightly modifies the electric potential of the ion and thus the energy of the transition levels and the wavelengths of the emitted photon is also modified.

This means that for each configuration of states of *spectator* electrons, there is a separate satellite line.

Near the Ly_α transition in hydrogen-like ions, the satellite lines corresponding to different states of the spectator electron are distinguished by the capital letters. In our measurements, we have focused on the J satellite which is produced by the decay from the state $2p^2 \ ^1D_2$ to the state $1s2p \ ^1P_1$.

The main diagnostic advantage of satellite lines is their sensitivity to plasma parameters (electron density and temperature) and their small reabsorption compared to the resonance line photons.

Each photon emitted by radiative decay can be reabsorbed by the inverse process, the *resonant photoabsorption*. The rate of this process (the number of photons of given energy absorbed per unit time per unit volume) is proportional to the density of ions in the lower state of the corresponding transition. This means that a photon emitted due

2. Elements of plasma radiation

to a decay of single excited ion into its ground state can be easily reabsorbed because the density of ions in the ground state is relatively large. In contrast, the satellite–line photons are usually weakly reabsorbed because the density of the excited ions, which are necessary for the reabsorption, is rather low.

To sum up, the photons of resonance lines are often reabsorbed and reemitted during the transfer from the plasma center to the detector (thus mostly carrying information about the region close to the plasma edge), while the satellite lines carry information directly from the place where they have been first emitted.

The multiple–excited ions can originate in several processes. One of them is the *dielectronic recombination*, when a free electron is captured into an ionic excited state and the remaining energy is transferred to the excitation of the bound electron. The other way is the *impact excitation* which may occur twice or more times within a short period of time, thus resulting in the multiple excitation of the ion.

This situation in a simulation of plasma with $T = 220$ eV and $n_i = 5 \times 10^{20} \text{cm}^{-3}$ is illustrated on Fig. 2.1. On the horizontal axis, there is a list of ionization and excitation states included in this simplified simulation – each bar presenting one state (g stands for ground state), and on the vertical axis, there is their fractional population in logarithmic scale. The horizontal arrows depicts the transitions relevant for the J–satellite, and different processes are identified. The J–satellite upper and lower states are marked with their names. The red bars depict the population given by LTE approximation, while the green ones represents the CR steady–state simulation.

2.3. Line shapes

The observed line shapes are often quite complicated, while the local emissivity and absorptivity profiles are usually treated as simple Voigt peaks (which represents the convolution of Gaussian and Lorentzian profiles). These profiles can have different widths and prospective Doppler shifts due to various plasma conditions, and therefore the line–of–sight integration over the plasma volume produces complicated resulting shape.

The emissivity and absorptivity peak width is constituted by several factors. The *natural* width, caused by the finite life–time of states, is relatively small and is seldom observed. The *microscopic Doppler broadening* mechanism is caused by the thermal velocities of ions, thus dependent on the ion temperature. In our conditions, the *Stark broadening* may be the dominant one. It is caused by the microfields of other nearby particles which perturbs the emitting ions potential, thus the broadening is dependent

2. Elements of plasma radiation

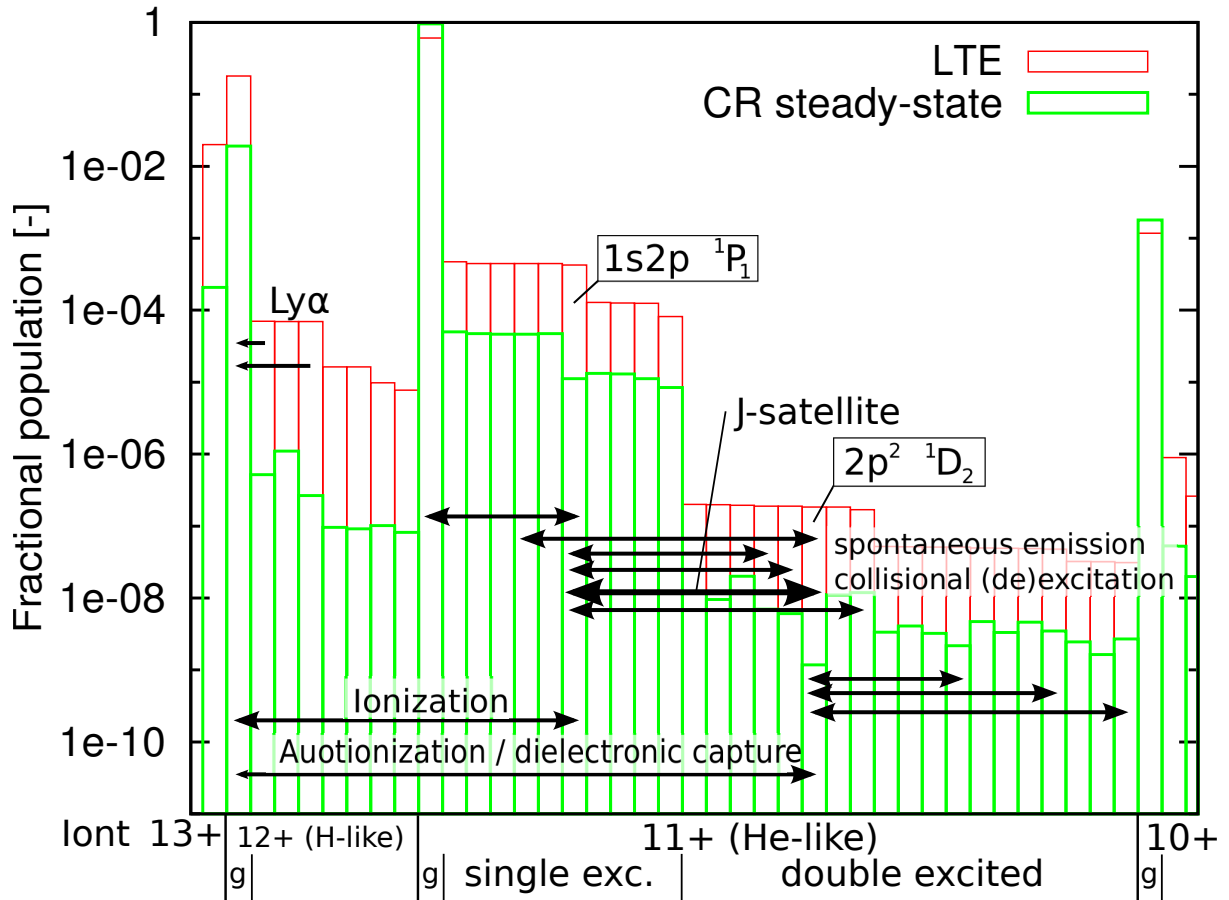


Figure 2.1.: Fractional population of various states in a plasma of $T = 220$ eV and $n_i = 5 \times 10^{20} \text{cm}^{-3}$ made using LTE assumption (red) and CR steady-state (blue). More description in text.

on the plasma density.

There are also other broadening mechanisms, like *macroscopic Doppler broadening* or *opacity broadening*, however these do not affect the local emissivity or absorptivity profiles, but are caused due to the line-of-sight integration of the radiation.

3. Double-foil experiments

In this section, the basic scheme of the double-foil laser-plasma interaction experiments is described as well as its instrumentation in our conditions. The spectra from these experiments constitutes the main data for the evaluation in the following chapters.

The principle of the experiment consists in laser irradiation of the target placed in a vacuum vessel, and collection and analysis of the x-ray spectra accompanying the laser-matter interaction. The target consists of two thin, intermediate-Z foils (usually 0.8 μm Al and 2 μm Mg) with variable spacing (usually 200 \div 500 μm).

As the laser beam impinges on the target, it produces a plasma on the first irradiated foil. The plasma jet expands perpendicularly to the foil surface at both its sides. With respect to the experimental configuration used, there are two possible scenarios:

1. The plasma jet collides with the relatively cold second foil.
2. The laser beam burns through the first foil and impinges on the second foil before the first-foil plasma reaches it. Consequently, there is already a plasma plume produced on the second foil before arrival of the plasma jet and we observe the collision of those two plasmas.

The occurrence of one of these scenarios depends mainly on the experimental geometry, on the thickness and composition of the first foil, and on the laser beam parameters.

In some experiments, an auxiliary counter-propagating laser beam can be focused on the second foil from the other side to preheat it and thus to vary the conditions of plasma interaction. The most relevant diagnostics for these experiments is based on the analysis of the emitted x-ray radiation. There can be several types of tools providing temporal, spatial or spectral resolution or its combinations.

The described experiments were performed at the PALS Research Center in Prague [3]. The PALS main laser beam is capable of delivering up to 1 kJ of energy at the fundamental wavelength 1315 nm which can be tripled to 438 nm. The pulse length is 250 \div 300 ps.

3. Double-foil experiments

Two main diagnostic tools installed were a vertical-geometry Johann spectrometer (VJS, described further) providing high-resolution spatially-resolved spectral data, and an x-ray streak camera combined with the slit providing spatially- and time- resolved measurements of plasma expansion.

3.1. Vertical-geometry Johann spectrometer

The vertical-geometry Johann spectrometer (VJS) is an x-ray spectrometer based on the principle of vertical dispersion. It provides a high-luminosity, high-resolution, 1-D spatially resolved spectral data. The basic principles of the VJS will be described, for further reference see [4], [5].

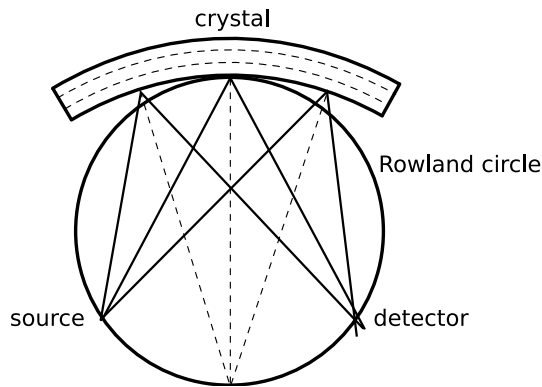


Figure 3.1.: Rowland circle scheme.

The main element of the VJS is a cylindrically bent crystal which defines a Rowland circle (RC). Neglecting the focussation defects, the Rowland circle scheme (Fig. 3.1) guarantees that any ray going from the point on this circle to the crystal is reflected to another point on the RC which is symmetrically located along the crystal axis.

This means that if the radiation is emitted from a line source lying on the RC, it is reflected and focused to the corresponding line on the RC, where a detector can be placed. In concrete experiments, neither the source, nor the detector are positioned perfectly on the RC. When using elongated sources, both the source and the detector are perpendicular to the central ray, connecting the relevant point on the RC with the crystal center.

The dispersion is realized in the vertical direction (i.e. perpendicular to the RC plane). It is based on the Bragg's law which states that only photons with the wavelength λ

3. Double-foil experiments

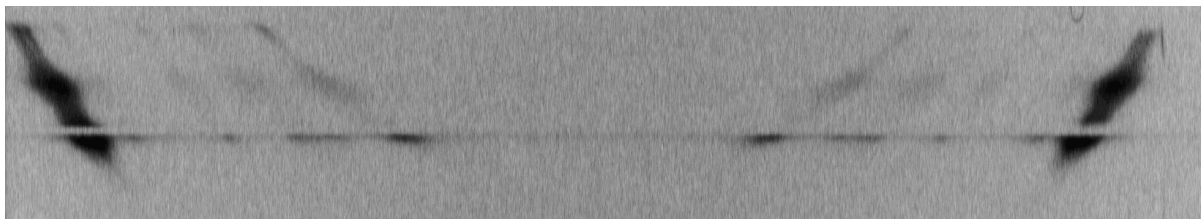


Figure 3.3.: Typical scanned film from the VJS with the spectrum recorded.

distances from the foil surface. Their special shape is due to the VJS geometry.

3.1.1. VJS spectra reconstruction

The films with spectral records (shown in Fig. 3.3) need to be digitized, calibrated and recalculated to get relevant spectral data.

The digitization can be performed by using a precise, but not easily available two-dimensional densitometer. As an alternative to this process, we have used a tabletop scanner EPSON PERFECTION V700 with the capability of scanning the films.

First, it was necessary to calibrate the scanner to the optical density which can later be recalculated to real exposures by using the known characteristic curves of the film.

To get this calibration, we scanned the calibration wedge delivered by the x-ray film producer (Kodak). The measured values stored in the tiff format were fitted with the logarithmic function (because of the logarithmic definition of the optical density). The resulting parameters of this fit were used for the spectra reconstruction. The found dependence of the optical density on the scanned tiff value is seen in Fig. 3.4, where the points denote measured data and the line denotes their logarithmic fit.

For handling the scanned films and the spectra reconstruction a special software package, the *VJS Analyser*, was developed as a part of my Bachelor work.

3.1.2. VJS Analyser

VJS Analyser[6] is a software package which I developed for the reconstruction and the analysis of the spectral data from the VJS. It is written in the Java language.

Only the main features and capabilities of this application are described here. The details of VJS Analyser can be found in its user manual in[6]. The illustrative picture of VJS Analyser in its spectra viewing mode can be seen in Fig. 3.5.

3. Double-foil experiments

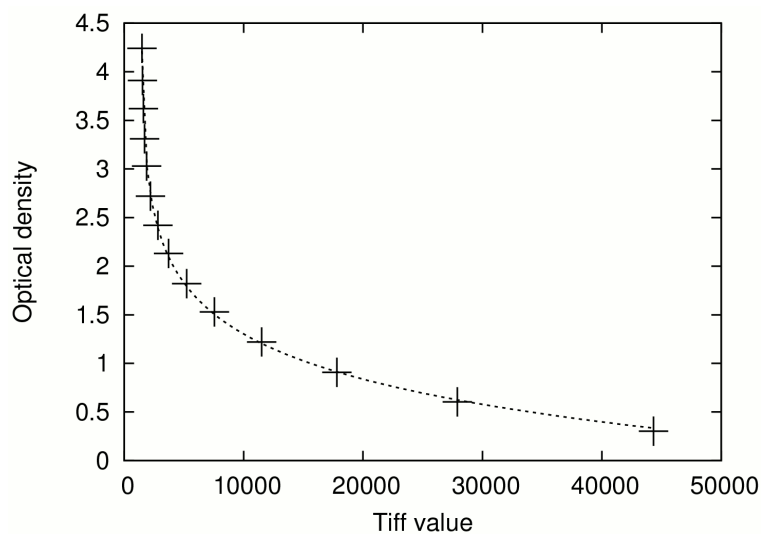


Figure 3.4.: Scanner calibration — the relation between the scanned tiff values and the optical density. Points represent the measured values and the line is the fitted calibration function.

The input of this application is a scanned film data file or an equivalent file from densitometer, in format of 16-bit gray-scale TIFF image.

The main functions of VJS Analyser include:

- Viewing and basic manipulation of 16-bit gray-scale TIFF images.
- Precise measurement of the spectral data tilt using correlation algorithm based on the data symmetry.
- Precise determination of the spectral line positions using the least square fit of the appropriate profile.
- Spectra reconstruction — conversion of the raw data into a set of calibrated spectra.
- Viewing and browsing of reconstructed spectra.
- Exporting the selected part of spectral data into a 2D plot suitable for elementary analysis or presentation.
- Exporting the spectral data into tables suitable for further analysis.

3. Double-foil experiments

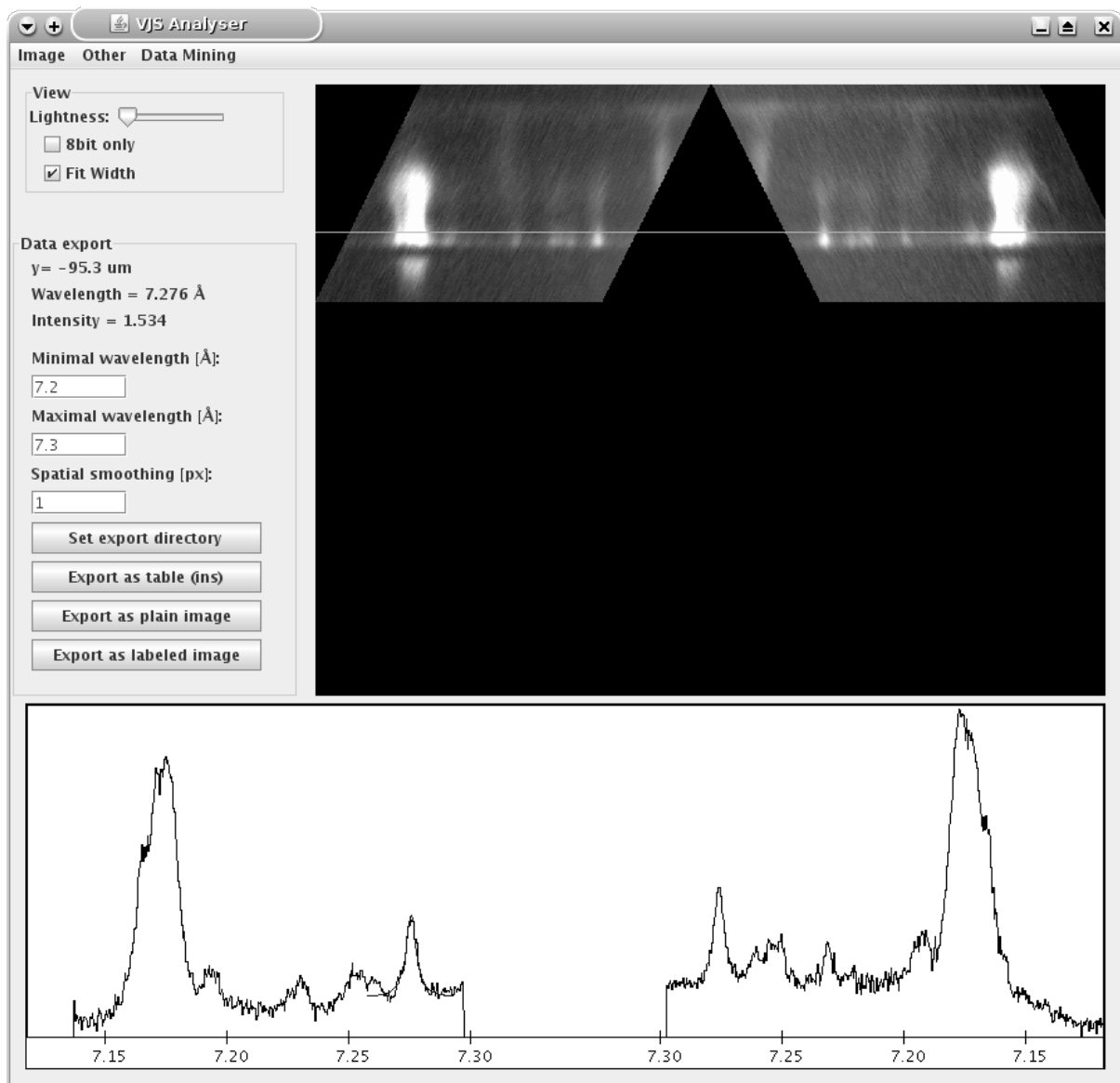


Figure 3.5.: Preview of the spectra analysing regime of the VJS Analyser.

4. Theoretical spectra

Theoretical x-ray spectra describing self-emission of hot dense plasma provide a very powerful tool for plasma diagnostics. The measured experimental data can be directly compared to a set of theoretical spectra and thus the free parameters of the simulation can be, therefore, estimated.

The crucial part of the spectra synthesis process is the calculation of plasma population distribution, i.e. the volumetric or fractional density of ions of given electronic state, which can be performed using alternate models for different regimes of plasma parameters. The Coronal equilibrium model (CE) gives the best results for diluted plasmas, while the local thermodynamical equilibrium (LTE) model is useful for dense, equilibrium matter. For our purposes, the intermediate Collisional Radiative model (CR, sometimes referred to as non-LTE or NLTE) is the only choice providing a possibility of handling non-equilibrium plasmas within huge range of densities[2].

4.1. Collisional–radiative model

The collisional–radiative (CR) model calculates the population distribution together with radiation, the first part of the model stands on the rate equation[7],

$$\frac{dn_i}{dt} = -n_i \sum_{j,j \neq i} W_{ij} + \sum_{j,j \neq i} n_j W_{ji}, \quad (4.1)$$

where n_i is the particle density of ions in the state i (the i -th ion population), and W_{ij} is the rate of transition between states i and j . The total transition rate W_{ij} is a sum of transition rates of all atomic processes comprised in the model,

$$W_{ij} = A_{ij} + C_{ij} + I_{ij} + DC_{ij} + \Gamma_{ij} + \dots, \quad (4.2)$$

where A_{ij} represents the spontaneous emission, C_{ij} the collisional excitation / deexcitation rate, I_{ij} is the collisional ionization, DC_{ij} denotes the dielectronic capture rate, and

4. Theoretical spectra

Γ_{ij} is for the autoionization. Details of selected processes are discussed in the section 4.3, but some other processes may be also involved.

The second part of CR model is the radiation transfer. It is governed by the equation[8],

$$dI(\omega, \Omega) = (\epsilon(\omega, \Omega) - \kappa(\omega, \Omega)) dx, \quad (4.3)$$

where dI is the incremental change of the directional spectral intensity with frequency ω in direction Ω , ϵ is the plasma emission coefficient and κ is the plasma absorption coefficient.

The emission coefficient is mainly given by the spontaneous emission, and the absorption one by the photoexcitation. Both coefficients are dependent on the population of emitting or absorbing levels. The transition rates of those processes are, on the other hand, dependent on the spectral intensity. This implies that the radiation transfer and the rate equations need to be solved together, usually by an iterative process.

4.2. Simulation codes

Three codes capable of CR plasma simulations have been investigated, FLYCHK, SPECT3D and CRETIN. Some spectra from the MARIA code by F.B.Rosmej were used for the comparison with our data, but the code itself is not available.

FLYCHK[9] is a freely available code with on-line functionality. It provides only zero-dimensional calculations, and the atomic levels are merged according to their principal quantum number n , thus the full level distribution, which is necessary to obtain detailed satellite structure, is not present. Those facts handicap the use of FLYCHK for our purposes.

SPECT3D IMAGING AND SPECTRAL ANALYSIS SUITE[10] is a commercially available code. It is distributed as a user-friendly application running in MS Windows. It includes the PRISM SPECT code for single-cell simulations and the SPECT3D code capable of 1D to 3D simulations. Both codes work with the same set of atomic data and the physical background. The version of this code available on July 2010 was not able to include velocities of various plasma cells into the simulations which was the main reason for us not to choose this code. Another disadvantage is that it is closed software, i.e. it can be used just as a “black box” with no detailed information about the physical background of the code.

CRETIN[11] developed by H.Scott is a freely available suite, distributed in a form of

4. Theoretical spectra

a Fortran source code. It strongly emphasizes the radiation transport and its effects on the plasma population. Its built-in atomic model is the same as the one in FLYCHK, i.e. with a limited use for us, but it can be used together with external models. The physical problem definition is done through rather a complicated text file, which is not so user-friendly, but it provides more possibilities for customization, and better integration with automated scripts.

We have chosen to use the CRETIN code and to create a suitable atomic model. Although this turned out to be rather a difficult task, it offers great flexibility and possibilities to understand, and potentially modify the whole simulation.

4.2.1. Comparison of CR codes

The first comparison, in Fig. 4.1, shows the MARIA spectra (blue lines) fitted on three experimental lineouts (black triangles) and a fit of the same data by PrismSpect simulations (red lines). The Maria spectra come from simulations with variable plasma thickness and gradients, while the PrismSpect ones assume a homogeneous plasma with thickness of 100 μm . The plasma parameters of spectra from both codes for all three cases are in Tab. 4.1.

With regard to the different basis of the simulations, the found parameters agree reasonably.

The second comparison, in Fig. 4.2, shows the same PRISM SPECT spectra as in Fig. 4.1 (red line), along with the data from CRETIN (green line), computed with the same parameters and geometry. The most significant difference is the strong reabsorption of the resonance line (at $\approx 7.17 \text{ \AA}$), caused by a different radiation transport algorithm. The agreement of the satellite structure is, on the other hand, satisfactory.

spectra	Maria		PrismSpect	
	T [eV]	$n_e [\text{cm}^{-3}]$	T [eV]	$n_e [\text{cm}^{-3}]$
(a)	300	3×10^{21}	460	1×10^{22}
(b)	700	3×10^{20}	760	1×10^{21}
(c)	220	$(1 \div 3) \times 10^{21}$	220	5×10^{21}

Table 4.1.: Parameters of simulational fits.

4. Theoretical spectra

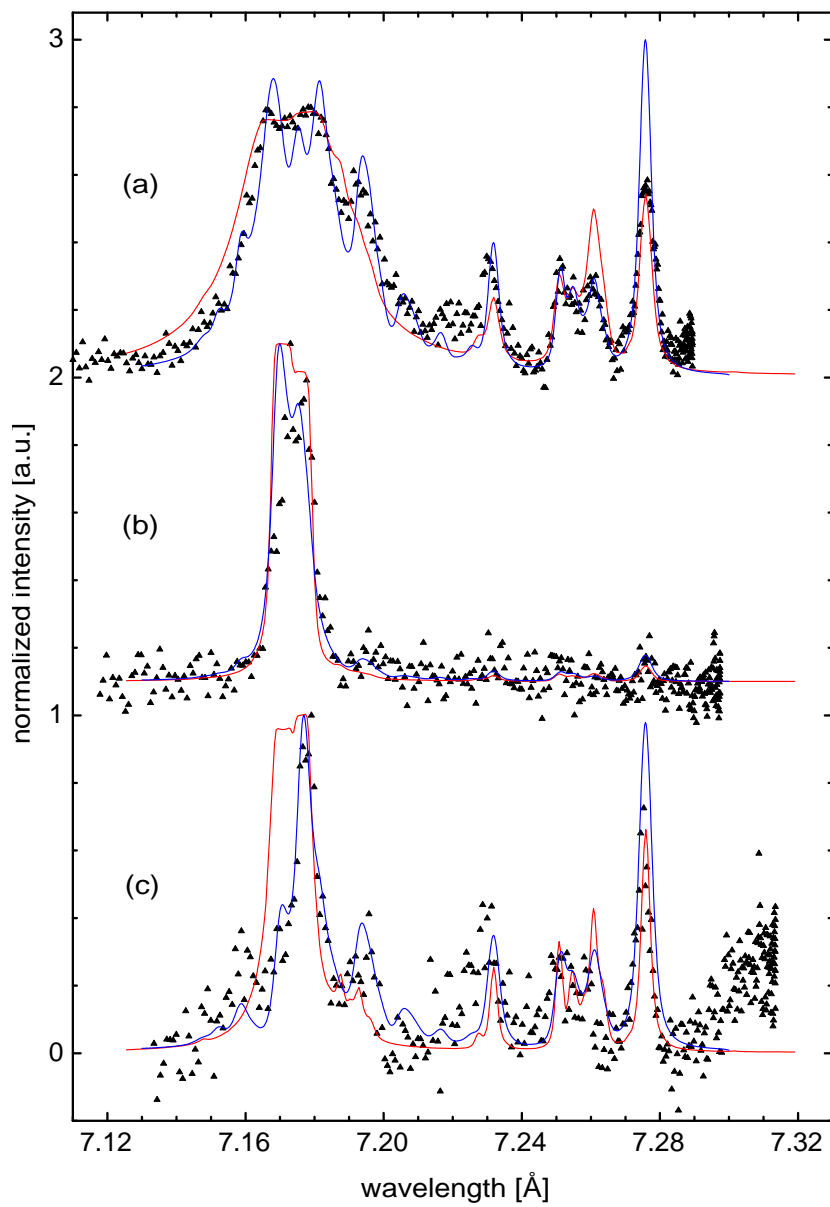
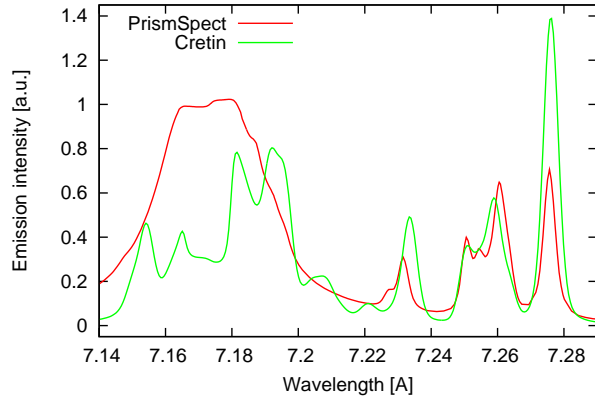
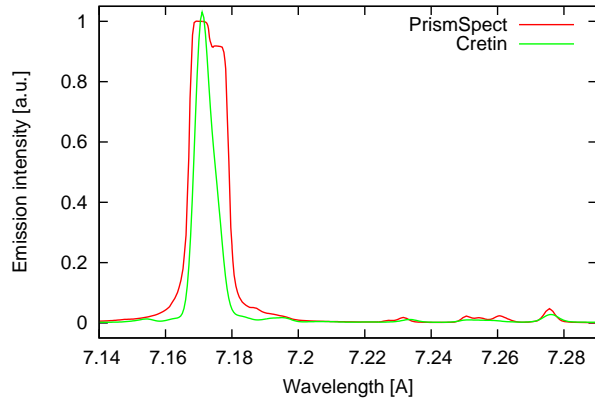


Figure 4.1.: Comparison of fitted theoretical profiles; Experimental spectra (black triangles) were fitted using the Maria code (blue line) and the PrismSpect code (red line).

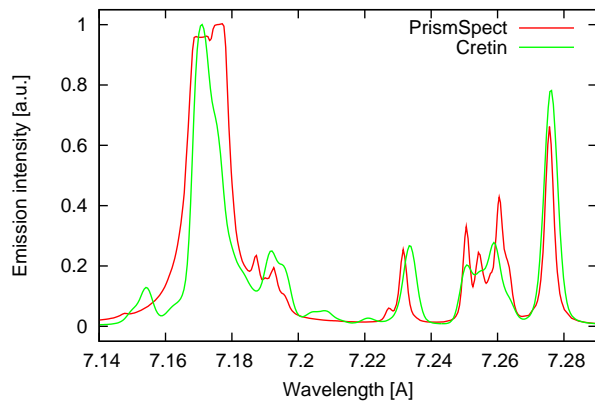
4. Theoretical spectra



(a)



(b)



(c)

Figure 4.2.: Comparison of spectra from PrismSpect and Cretin for various parameters, as described in Tab. 4.1

4.3. Atomic model

By an atomic model we mean a data file containing all the atomic data necessary to run the CR simulation. Since the built-in model in Cretin is not detailed enough, we had to gather all the data and formulate them into an format readable by Cretin, i.e. a plain text file well described in the Cretin manual. Its current size is approximately 2 MB. The data contained in this file is discussed in the next paragraphs.

The data consists of two parts, the energy levels and atomic transitions between those levels. The elementary data, i.e. energy levels and Einstein coefficients, can be found tabulated, but the precise rates for other processes need to be calculated using a proper atomic code. Three of these codes had been investigated, the COWAN code, FAC, and HULLAC, but only the last one provided coefficients for the collisional excitation with sufficient precision, so HULLAC has been chosen to build our model. The list of all included processes and their inverse ones is summarized in Tab. 4.2. Note that the rates of the pair of the processes are coupled together with the detailed balance principle[2], so the rate of only one of these is needed in the model.

4.3.1. Levels

The atomic levels included are those of Al IX to Al XIII (Be-, Li-, He-, H-like and fully ionized atoms), from ground states up to $n = 4$ states. In He-like atoms, the double-excited states are included. The list of included states defined by their quantum numbers n and l can be seen in Hullac input files in appendix A, where each line in the DATA section represents one subshell. Hullac incorporates all configurations within those subshells into the model.

In the atomic model, each level needs to be supplied by its energy above the ground

Direct process	Inverse process	Data file section
Spontaneous decay	Photoexcitation	rad_rate
Electron collisional excitation	El.coll. deexcitation	cxbbtc
Autoionization	Dielectronic capture	aut_rate
Electron collisional ionization	3-body recombination	colon
Photoionization	Radiative recombination	phot_cs

Table 4.2.: List of atomic and corresponding inverse processes included in the model and their locations in the Cretin atomic model file.

4. Theoretical spectra

state of the current ion (in eV), and by its statistical weight g , i.e. by the degeneracy of this state.

4.3.2. Spontaneous decay / photoexcitation

The rate of spontaneous decay is given by the Einstein A -coefficient [s^{-1}] which gives the number of spontaneous transitions of the atom in the upper state undergone in unit time. The formula[2]

$$A_{u \rightarrow l} = 2c \frac{e^2}{(\hbar c)^2 m_e c^2} (\Delta E)^2 f_{u \rightarrow l}, \quad (4.4)$$

directly relates this coefficient to the *oscillator strength* f . $u \rightarrow l$ means transition from the upper to the lower state, ΔE is the energy difference between the levels, other symbols are common physical constants.

The oscillator strengths and consequently also the Einstein coefficients can be easily obtained from all atomic codes mentioned above.

4.3.3. Electron collisional excitation / deexcitation

The electron collisional (impact) excitation is a process when a free electron hits an atom in a (lower) state and excites it without being captured. It is obvious that the cross-section σ of this process is dependent on the collision energy ϵ . In order to get the rate of this process in plasma, the cross-section is integrated over Maxwellian distribution with given electron temperature. Unfortunately, the dependency of this rate on temperature can not be easily and precisely expressed as an analytical function with a reasonable parametrization, and performing the cross-section calculation within the CR solver would be computation costly.

There are also some semi-empirical formulae for the excitation rate, mainly based on the oscillator strength f , but they do not provide sufficiently accurate results.

The best solution found was to use the BBTC fit[12], proposed by the author of HULLAC, which maps the function $\sigma(\epsilon)$ using a specific rational function to a dimensionless *mapped oscillator strength* z which is then evaluated in 9 fixed points. Altogether with the mapping parameters, there are then 13 coefficients which can be used in the CR-solver to reconstruct the cross-section $\sigma(\epsilon)$ precisely and then perform its integration over Maxwellian distribution effectively.

4.3.4. Electron collisional ionization / recombination

The situation in the electron collisional ionization and recombination is analogous to the electron collisional (de)excitation. For this process, the older formula of Goett et al[13] fitting the cross-section is sufficient, it is, therefore, used instead of the more complicated BBTC fit.

4.3.5. Autoionization / dielectronic capture

The autoionization is a process describing spontaneous ionization of the double-excited state with the energy above the ionization limit. One of the excited electrons decays into a lower state, usually the ground one, while the other one gets into the continuum, carrying the residual energy. The inverse process is a dielectronic recombination, when a free electron is captured into the excited state, transferring the extra energy into the excitation of a bound electron. This is of great importance because it significantly increases the population of double-excited states.

The autoionization rate, usually denoted as A_a or Γ , is directly calculated by using the atomic codes and passed into the model.

4.4. PALE Hydrodynamics

The hydrodynamic simulation needed for the calculation of synthetic spectra were performed independently on the ion populations and radiation, which means that prospective fine effects of plasma-emitted radiation back-coupling were neglected.

All the hydrodynamics data describing the plasma evolution was overtaken from the results of the Prague Arbitrary Lagrangian Eulerian (PALE) code[1], modeling was provided by courtesy of R.Liska. The spectral postprocessing discussed in the next chapter is based on one the PALE simulation, made in 2-D rz geometry for the aluminium foil with the quotidian equation of state (QEOS) and variable mean ionization. The 0.8 μm thick foil located at $z = 0$ consists of 100×40 mesh points, and is irradiated by a laser beam coming from the positive z direction with a focal spot with the 80 μm diameter on the foil. The laser frequency is 438 nm (to simulate the PALS 3ω), energy 78 J, FWHM pulse length 300 ps. Laser irradiation starts at $t = 0$, thus the laser pulse maximum is at $t = 150$ ps. The time steps were set to 5 ps. The ion density and temperature distributions in the deformed mesh in time $t = 200$ ps are shown in Fig. 4.3.

4. Theoretical spectra

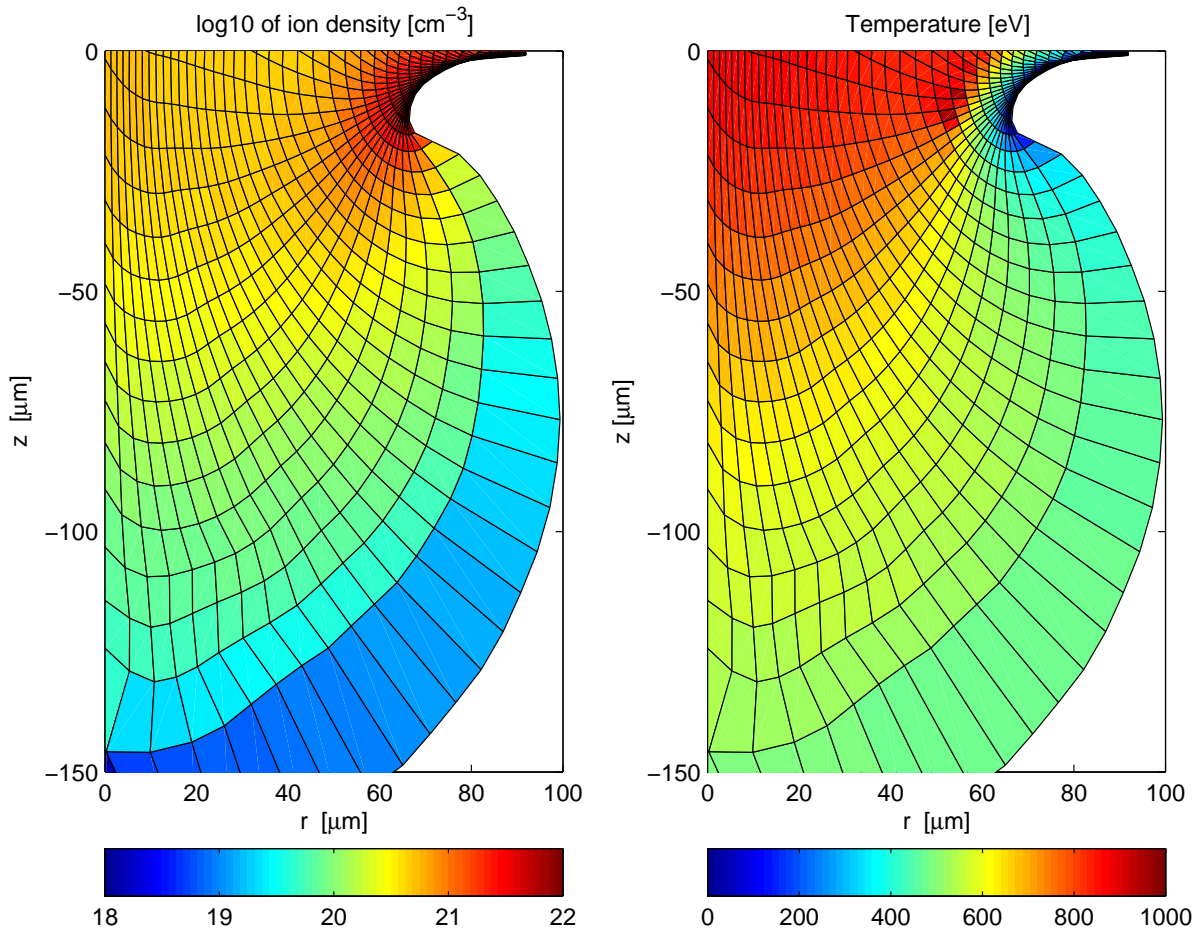


Figure 4.3.: Ion density and plasma temperature in the deformed Lagrangian mesh behind the foil in the PALE simulation for time $t = 200$ ps.

4.5. Time-dependent and steady-state regimes

The CR model can be used either in steady-state or time-dependent regimes.

In the simpler *steady-state* regime an assumption is made that throughout the simulation and for all plasma elements the populations are given by equation

$$\frac{dn_i}{dt} = 0. \quad (4.5)$$

Thus each time step is independent on the other one.

In the *time-dependent* CR model, the plasma population is first initialized using LTE or CR *steady-state*, and then it evolves continuously with time within each plasma cell. The evolution of population is governed by the equation (4.1) with the transition rates W_{ij} calculated for given plasma parameters, thus the population in given time can be

4. Theoretical spectra

strongly dependent on its preceding evolution.

In order to solve the question of how fast changes in plasma parameters can be treated with the *steady-state* simulation, and for which phenomenon a *time-dependent* solution is necessary, a simulation was performed to get an estimate for the stabilization time of the steady-state simulation.

The initial population in this simulation has been set using the *steady-state* CR for a plasma of $T = 220$ eV, $n_i = 5 \times 10^{20} \text{cm}^{-3}$ and thickness $L = 100 \text{ }\mu\text{m}$, then a sudden change of temperature has been made to $T = 250$ eV and the consequent evolution of the spectrum has been observed. It has reached its stabilized shape just after approximately 300 ps, as can be seen in Fig. 4.4. The simulation indicates that the estimate of the temperature change of order of magnitude 100 eV/ns could be treated in a steady-state regime.

To compare this value with a typical evolution of the plasma temperature within one cell of the hydrodynamic PALE simulation (section 4.4), here we present Fig. 4.5. The speed of the temperature change is approximately 50 eV/ps, about three orders of magnitudes

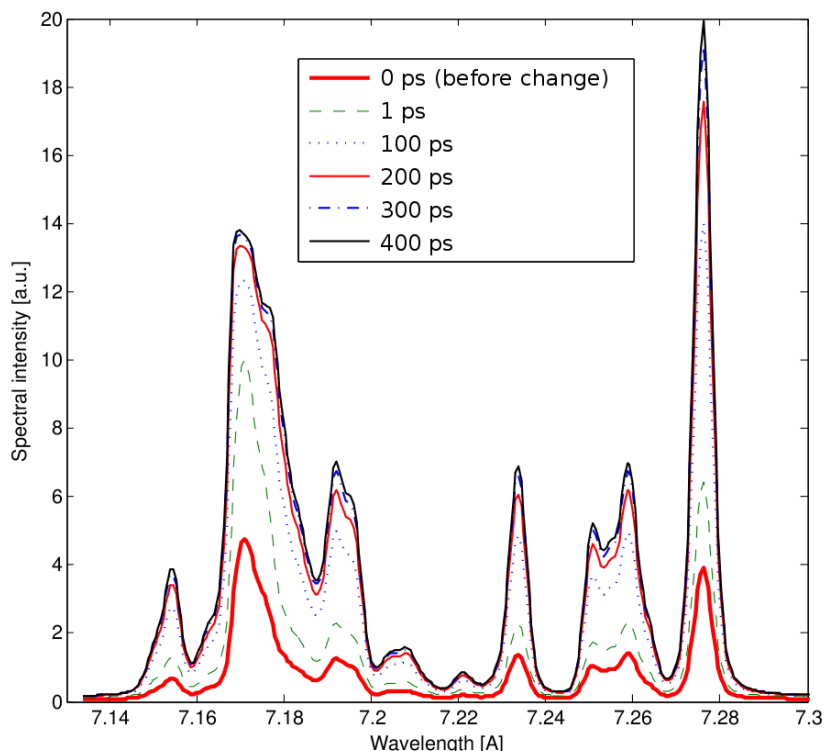


Figure 4.4.: Stabilization of spectra in the time-dependent regime. The thick red line shows a plasma of temperature 220 eV, the other lines depicts the situation in various time intervals after a sudden change of temperature to 250 eV.

4. Theoretical spectra

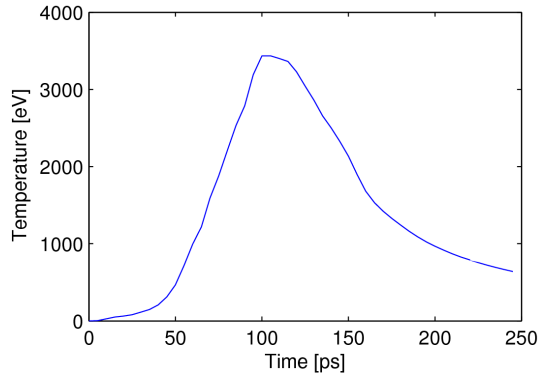


Figure 4.5.: Temperature evolution within one cell of the PALE simulation.

higher than the above mentioned criterion, thus, obviously, treating those simulations with a steady-state regime would be inappropriate.

Another argument for application of the time-dependent model again follows from the PALE simulations; for both regimes, we compare the time evolution of ionization states. For this purpose, the on-axis cell near the rear surface of the laser-irradiated foil was selected, the ion density and temperature in this cell are shown in Fig. 4.6. The population distribution in this cell was evaluated using time-dependent and steady-state models, the evolution of populations of different ionization stages are shown in Fig. 4.7 and Fig. 4.8. During the heating — ionizing phase, i.e. up to 150 ps, (which corresponds to the laser pulse maximum), both cases behave very similarly, partly because of the high density, which means shorter collision times and a faster adaptation to the temperature increase. On the contrary, there is a huge difference during the cooling — recombining phase. The steady-state ionization (Fig. 4.7) shows the ionization relevant to current temperature irrespective of previous evolution. Consequently, for the region between $t = 250 \div 450$ ps, where the temperature is decreasing from 400 eV to 100 eV, the He-like ions significantly dominant. On the other hand in the time-dependent simulation, the collisions in diluting plasma are becoming more rare and the stabilization time grows. The plasma does not significantly change its ionization since reaching the maximum temperature.

This difference is even more important if we realize that the measured spectra are produced mainly by the He-like ions, an abundance of which shows the largest difference between both cases. On the other hand, in the time after ≈ 300 ps, the axial position of studied cell is out of the reach of the detector, and its density is relatively low, so it probably does not significantly contribute to the produced spectra.

4. Theoretical spectra

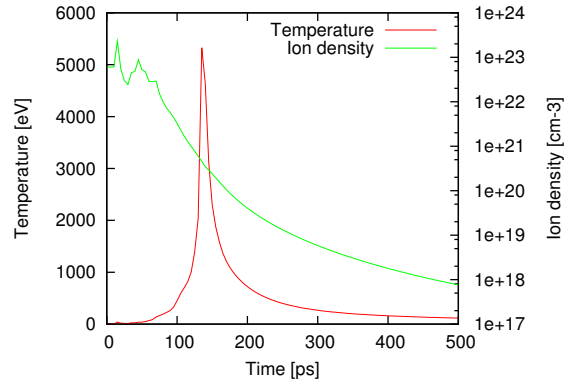


Figure 4.6.: Parameters of the cell selected to preview the ionization evolution.

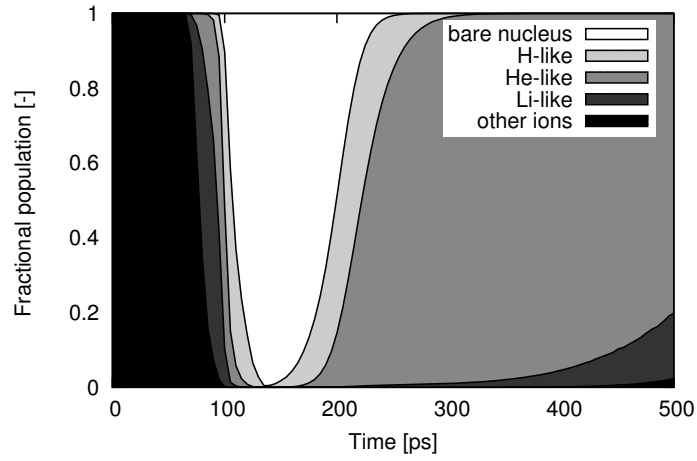


Figure 4.7.: Ionization evolution in steady-state regime.

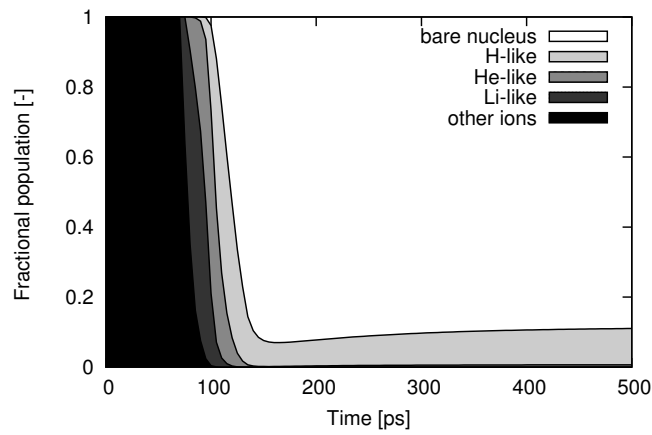


Figure 4.8.: Ionization evolution in time-dependent regime.

4.6. Data flow

All codes and data files needed for the hydrodynamic data postprocessing and their relations are to be discussed in this section. The overall process is shown in the diagram in Fig. 4.9.

The ANGINP files (Appendix A) defines the ionization and excitation states, and the types of atomic processes included in the model. The HULLAC code then calculates all necessary atomic data, which are converted into a format readable by CRETIN via the HULLAC2CR code.

From the PALE hydrodynamics code we obtain the binary .NC file containing the output data. This file is converted into an XFILE, an input format defined by CRETIN, by using script in MATLAB.

The XFILE and the atomic model are referenced in the GENERATOR FILE (Appendix B) which also defines the simulation geometry, parameters, desired output and all necessary settings. These files are all the input data needed by CRETIN to produce the desired output, i.e. the synthetic spectra to be compared with experimental observations. Finally, the graphical output presented in this thesis is produced from the spectra by using scripts written in JAVA.

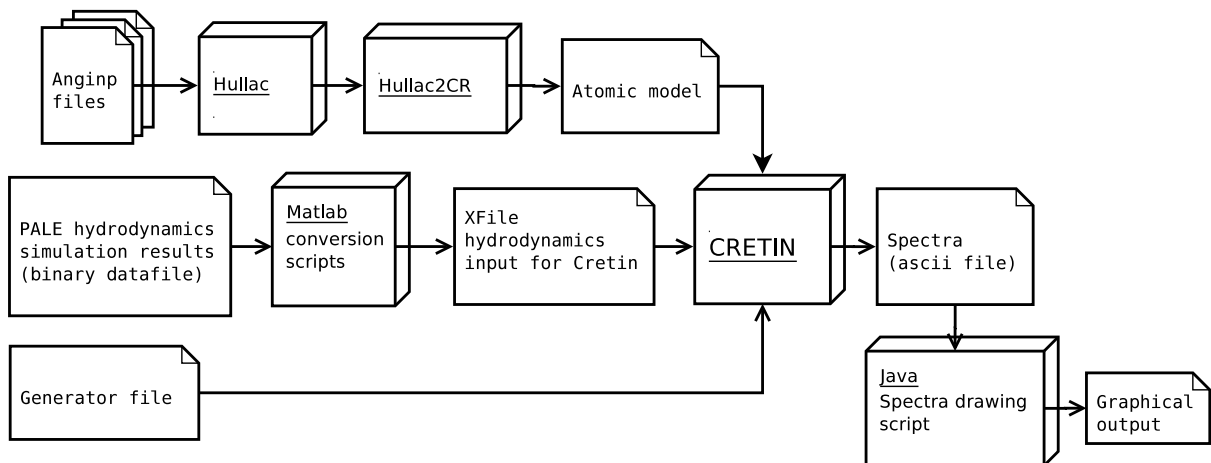


Figure 4.9.: Data-flow diagram of the spectral postprocessing of PALE hydrodynamics.

5. Hydrocode postprocessing

5.1. Work overview

Hydrodynamic data postprocessing and theoretical spectra synthesis represent rather a difficult and subtle processes. Considering this, a plan of various simulations starting with a relatively simple one and extending up to complex ones has been made. Each step in this plan consists in inclusion of additional well-defined features, so the two consequent simulations can be compared and the differences discussed. This slow and detailed approach also facilitates better understanding of various aspects of the simulation.

The table of simulations is shown in Tab. 5.1, the check mark (✓) means that a feature is added, the bullet (●) shows that this feature needs to be added because it is interlinked with another one.

The physical features to be consecutively added include:

- *Time-dependent regime*: If included, the whole simulation is treated using the time-dependent approach, otherwise the steady-state assumption is applied throughout the simulation.
- *Radial profile*: If selected, the radial (perpendicular to laser beam axis) profile of plasma temperature and density is included, otherwise only the on-axis parameters are used and the simulation proceeds with a single-cell approximation in the radial direction.
- *Velocities*: If selected, both radial and axial velocities are included in the simulation. Otherwise, these velocities do not pass into Cretin, thus disabling the macroscopic Doppler effects.

The following features are rather technical aspects of the simulation, they should not significantly affect the results, but need to be treated carefully to make sure the simulation runs properly:

5. Hydrocode postprocessing

Feature	Simulation name							
	A	T1	T2	B	T3	C	D	
Time-dependent regime				✓	✓	✓	✓	
Radial profile						✓	✓	
Velocities							✓	
data dimension	0D	1D	1D	1D	1D	2D	2D	
geometry	slab	xy	xy	xy	rz	rz	rz	
using detectors		✓	•	•	•	•	•	
Lagrangian coordinates			✓	•	•	•	•	

Table 5.1.: Plan of hydrodynamic data postprocessing simulations.

- *Data dimension*: Dimensionality of the input data file (XFILE) for Cretin. (0-D means there is a spatially resolved set of single-cell simulations.)
- *Geometry*: Geometry of the simulation definition in Cretin. It can be *slab*, *xy* or *rz*.
- *Using detectors*: The plasma radiation is evaluated using the *detector* command in Cretin, i.e. the definition of the position and the angle of spectra observation, otherwise the simpler *isp+* command is used, which connects the output emission to a given cell.
- *Lagrangian coordinates*: The original Lagrangian coordinates from the PALE simulation are transferred into Cretin, otherwise the data are interpolated into the Eulerian ones.

The simulations $T1 \dots T3$ were performed in order to check the correct implementation of the added features. Since they worked properly, they are not presented here. The results of other simulations are discussed below.

The used coordinate system follows the hydrodata: the problem has a cylindrical symmetry with the axis (the z -coordinate) defined along the laser beam axis. The laser beam impinges the foil from the positive z direction.

5.2. Case A: The steady–state on–axis simulation

The most simplified simulation *A* consists of a 1–D plasma column along the laser beam axis with the lateral extent of 100 μm . Although the plasma parameters evolve in time, the ion populations are calculated using the CR steady–state approximation.

Even for this simplest simulation we get spatially–resolved, time–integrated spectra (Fig. 5.1) which are qualitatively in a good agreement with experiments. Several new and interesting conclusions can be deduced from the Z - T diagram shown in Fig. 5.2. This diagram depicts the integrated emission intensity of the Ly_α resonance line ($7.15 \div 7.20 \text{ \AA}$), in red, and its satellites ($7.22 \div 7.30 \text{ \AA}$), in green color, with the temporal (along the X -axis) and spatial (along the Y -axis) resolution. Both intensities are normalized independently with respect to each other, and are mapped to the colors in the logarithmic scale over three orders of magnitude.

In the beginning of the simulation, the emission can be seen from a very narrow (in z -dimension) region, moving backwards with plasma. This emission from the laser-irradiated foil is much more intense than the later one, produced by the more diluted plasma plume, stretched in time ($150 \div 400 \text{ ps}$) and space ($0 \div -70 \mu\text{m}$).

The spatial profiles of temperature and density are indicated in Fig. 5.3 for time $t = 60 \text{ ps}$. The dense foil is clearly distinguished at $z \approx -6 \mu\text{m}$, which corresponds to the strong emission seen at this time and position at Fig. 5.2.

Another effect present in Fig. 5.2 is the time variation of the spectra character during the second phase: the resonance line (red) is emitted earlier than the satellites (yellow) — this can be explained by the temporal decrease of temperature: The higher temperature in the earlier phase of the plasma evolution means the higher population of the H-like ions which produce the resonance line. During the later lower temperature period, the He-like ions are the most abundant species, producing the satellite lines. Note that the yellow color means that both the resonance line (red) and the satellite lines (green) are present, thus mixing the colors into yellow.

The effect of two distinctive emission regimes is also seen from the temporarily resolved spectra synthesized for different z positions. In Fig. 5.4, corresponding to the distance of 30 μm behind the foil, a very short and intensive emission is seen at $t \approx 120 \text{ ps}$, followed by a relatively weak signal in the time period between 200 and 450 ps. The first peak is emitted by the target foil itself, which is being moved backwards and heated to several hundreds eV at relatively high ion density, .

On the other hand, Fig. 5.5 showing the emission calculated for $z = -50 \mu\text{m}$, predicts

5. Hydrocode postprocessing

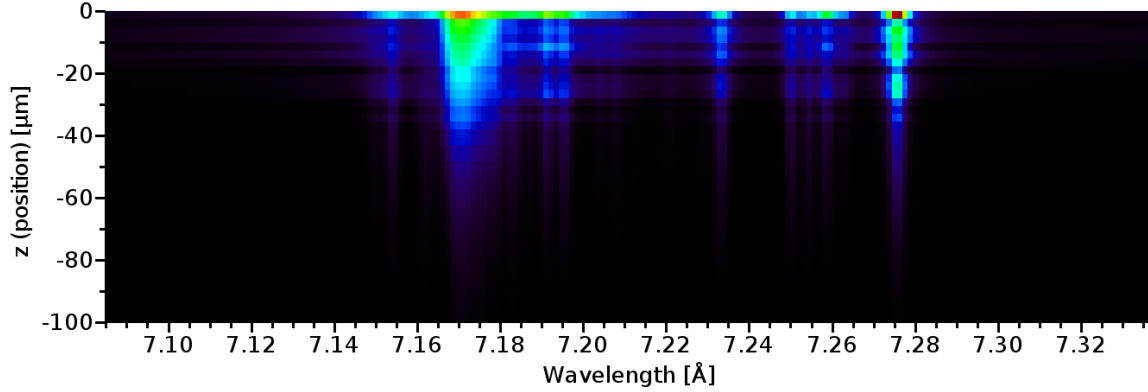


Figure 5.1.: The spatially-resolved time-integrated spectra of the Ly_α group for the *A* simulation.

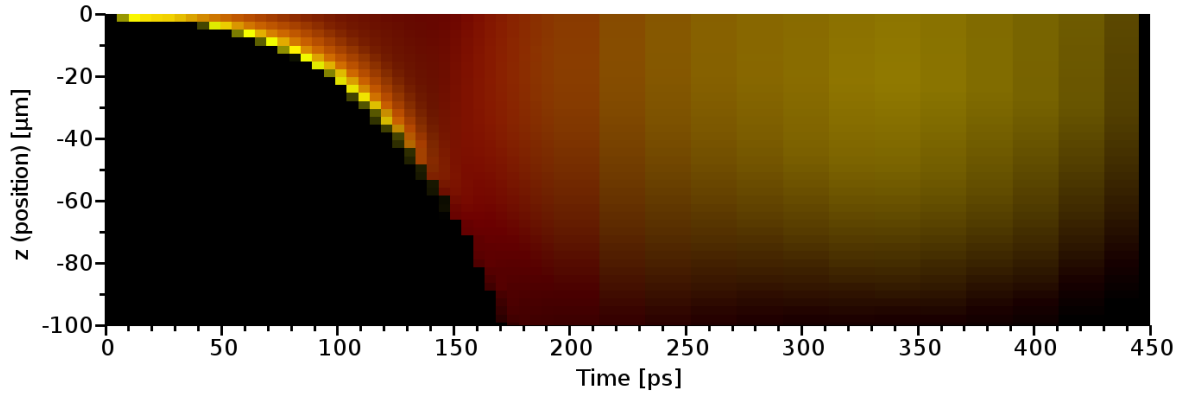


Figure 5.2.: The spatially- and time- resolved emission intensity (Z - T diagram) of the *A* simulation. The red color corresponds to integrated intensity of the resonance line, the green one to the satellite-lines.

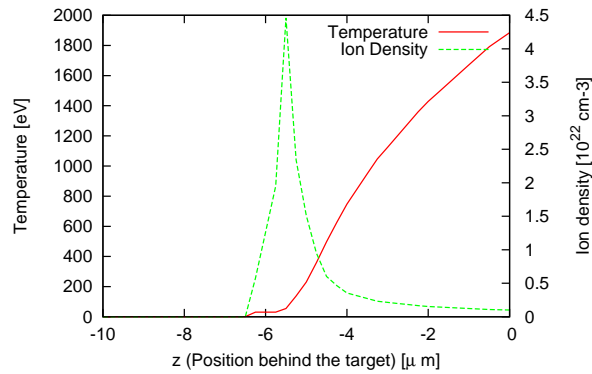


Figure 5.3.: Temperature and ion density depending on the z -coordinate for time $t = 60$ ps

5. Hydrocode postprocessing

fairly continuous intensity in the time period $T = 200 \div 450$ ps, with the resonance line appearing distinctly earlier than its satellites.

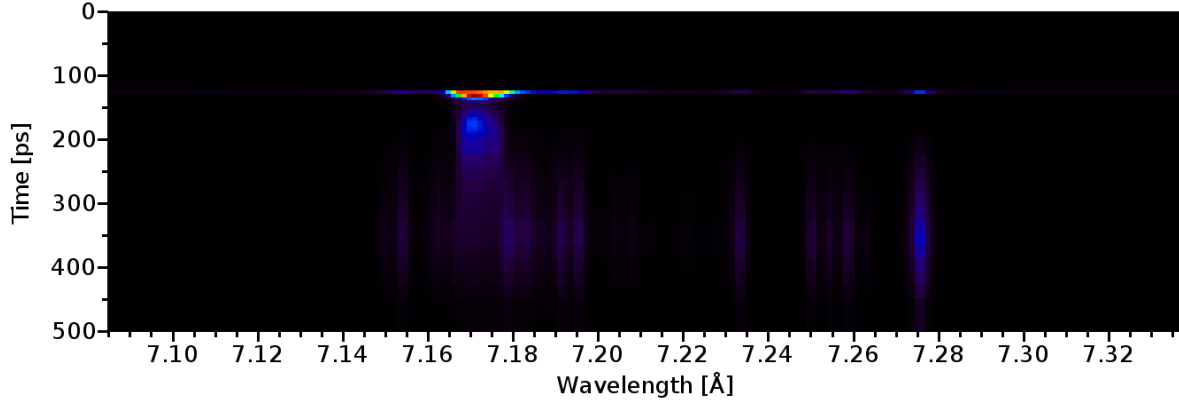


Figure 5.4.: The time resolved spectra for the A simulation at $z = -30$ μm .

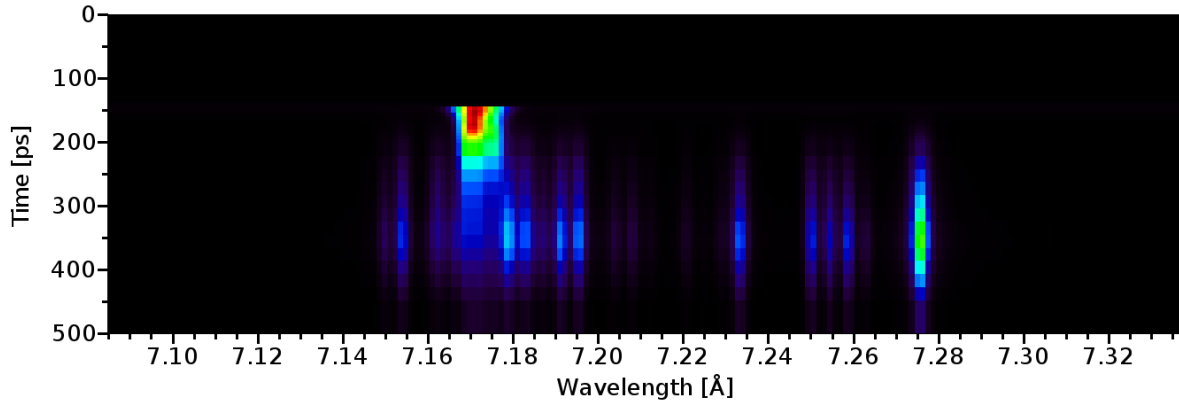


Figure 5.5.: The time resolved spectra for the A simulation at $z = -50$ μm .

5.3. Case B: The time-dependent on-axis simulation

In this simulation, only the Lagrangian cells positioned on the z -axis were taken into account, their lateral width was again fixed to be $100\ \mu\text{m}$ and their Lagrangian character had been kept to ensure correct plasma convection which is necessary for the time-dependent population kinetics used. Obviously, this simulation has the same geometry as case *A*. The spatially-resolved time-integrated spectra and the Z - T diagram (as described in the previous section) are shown in Fig. 5.6 and Fig. 5.7.

The most significant difference compared to the steady-state *A* simulation is the suppression of the delayed emission further from the target (at $t > 200\ \text{ps}$ and $z < -60\ \mu\text{m}$), which is seen in the Z - T diagram. The smoother initial radiation from the dense foil region is probably due to numerical reasons.

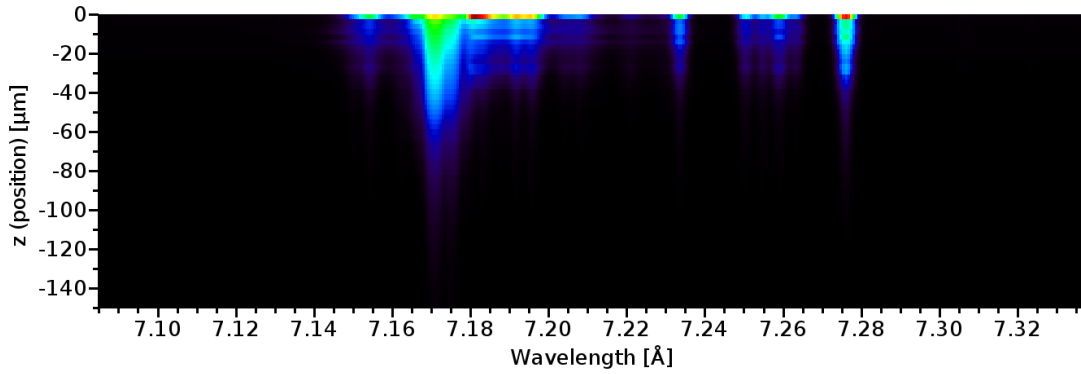


Figure 5.6.: The spatially-resolved time-integrated spectra for the *B* simulation.

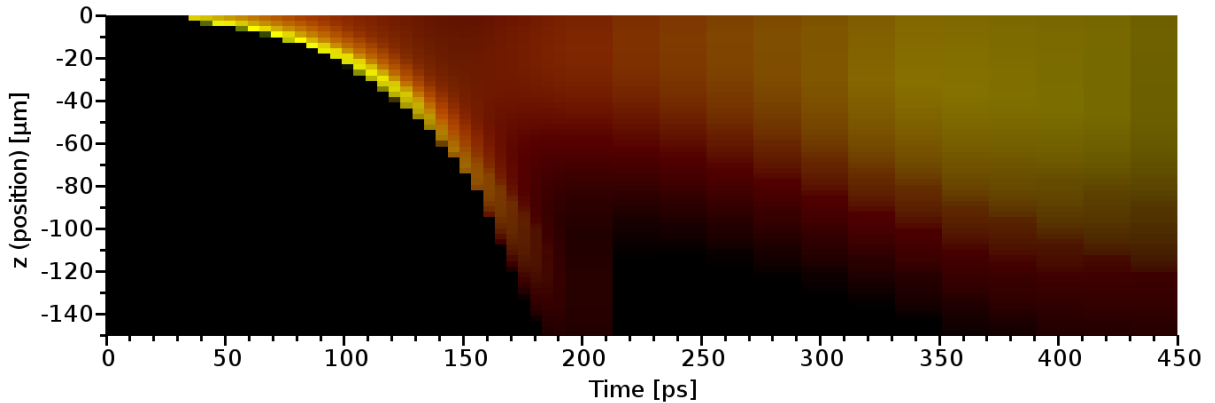


Figure 5.7.: The Z - T diagram of the *B* simulation. The red color corresponds to the integrated intensity of the resonance line, the green one to the satellite-lines.

5.4. Case C: Full geometry, no velocity effects

This time-dependent simulation incorporated a 2-D mesh of Lagrangian cells from PALE, thus it is much closer to the real experimental geometry.

Because the current version of Cretin can not handle the fold profiles of the deformed meshes properly, the outer cells from the simulation had to be removed. The meshes before and after this modification are drawn in Fig. 5.8. Since the observed radiation is emitted mainly from the central (near-axis) region, the removal of plasma edges should not significantly affect the spectra.

The time-integrated emission spectra from this simulation were not much different from those in the case *B*. The main variation can be found for the early phase of the plasma evolution in the near-foil region. The radiation there is intensified due to deflection of the hot dense foil, which is now emitting to the wider z area. On the contrary, the foil was represented only by single z -position in the on-axis simulation.

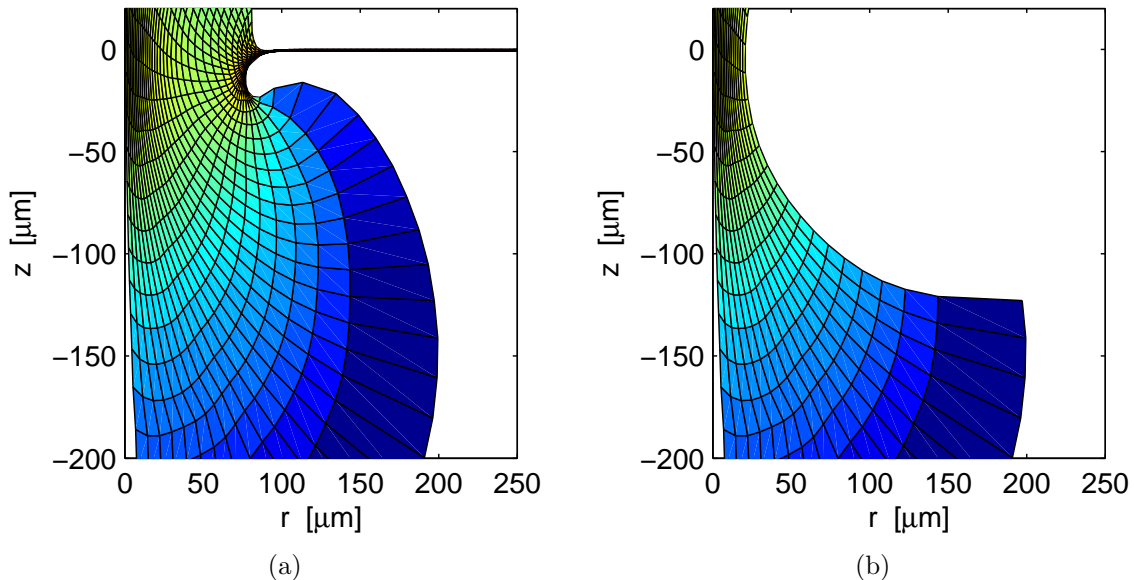


Figure 5.8.: The original deformed mesh (a) from the *PALE* simulation for time $t = 275$ ps, and mesh modified for postprocessing (b) where the radially outer cells have been removed to avoid geometry difficulties. (Colors are mapped to logarithm of density.)

5.5. Case D: Full geometry simulation with ion velocities included

The D simulation is analogous to the case C, but macroscopic plasma velocities had been added, and the Doppler shifts of line profiles are thus incorporated into the calculation. This essentially affects the emitted spectra (Fig. 5.10). On the contrary, the Z - T diagram in Fig. 5.11 does not change much compared to the previous simulation.

The inclusion of velocities, especially their radial component, results in two significant effects:

- Macroscopic Doppler broadening.
- Relative decrease in the satellite lines intensity.

Both effects can be seen in Fig. 5.9, where spectra corresponding to the position $z = -40 \mu\text{m}$ behind the foil and time $t = 235 \text{ ps}$ from simulations C and D are compared. The macroscopic Doppler broadening is caused by various Doppler shifts of different elements of expanding plasma, and it is discussed in [14].

The suppression of the satellite-line intensity in the region further behind the foil is more difficult to explain. Tentatively, this is ascribed to redistribution of the energy level populations due to radiative transfer effects. This is to be investigated in further work.

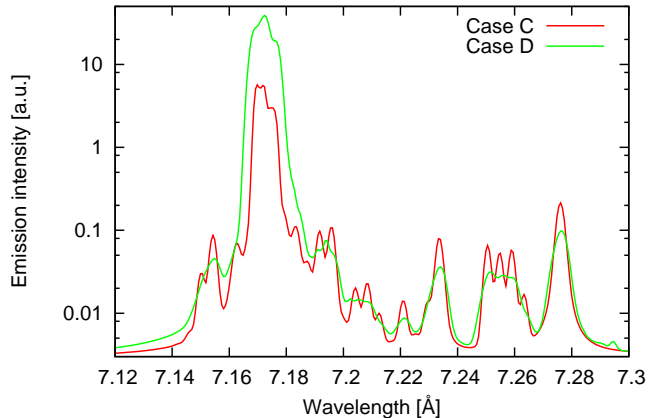


Figure 5.9.: Spectra from C and D simulations for $t = 235 \text{ ps}$ and $z = -40 \mu\text{m}$ in logarithmic scaling.

5. Hydrocode postprocessing

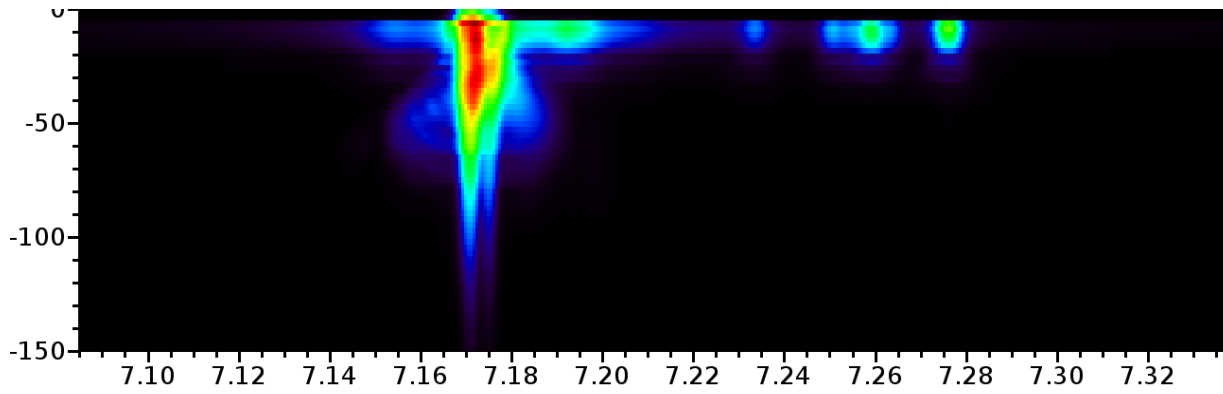


Figure 5.10.: The spatially-resolved, time-integrated spectra for the D simulation.

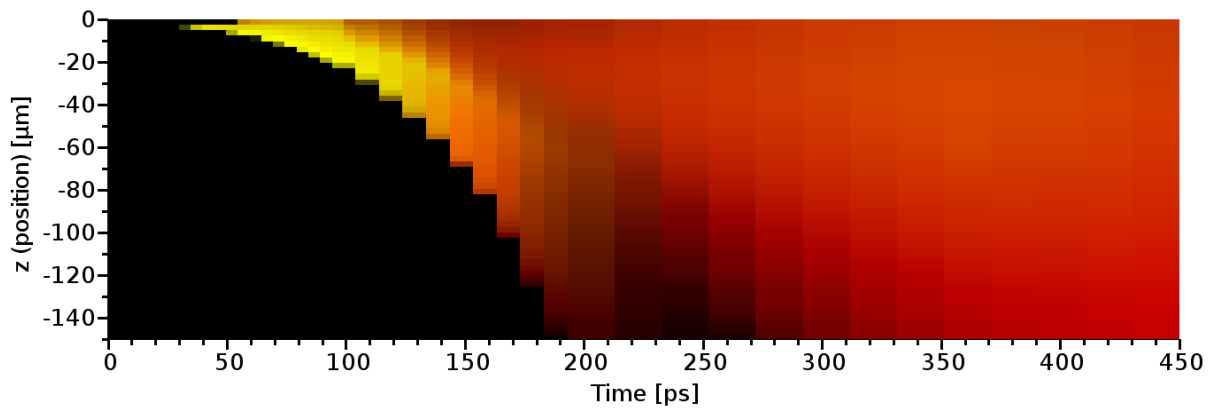


Figure 5.11.: The Z - T diagram of the D simulation. The red color corresponds to the integrated intensity of the resonance line, the green one to the satellite-lines.

6. Sample application in experimental spectra evaluation

The evaluation of the experimental observed spectra directed at mapping of macroscopic plasma characteristics is a different task when compared with the hydrocode data post-processing. For this purpose, a set of simulations with properly chosen free parameters is to be performed and subsequently, these parameters are adjusted to get the best fit with the experimental data.

In the ideal case, the needed set of simulations should be provided directly from the hydrocode coupled with the postprocessor. This is currently not feasible with respect to computation time, this very complex task will be a subject of next studies. In the first approximation, we have applied a relatively simple evaluational procedure described below.

6.1. Methodology

The single-time steady-state simulation is performed by using information on plasma gradients following from the PALE simulation. Sample gradients of T , n_i , u_r were calculated for time $t = 200$ ps and $z = -50$ μm , and scaled to fit the experiments.

The scaling of profiles and spectra generation is performed using scripts written in JAVA, the search for the best fit benefits from the COMPSPECT code developed to provide fast and easy-to-perform comparison of the experimental spectra to the set of theoretical ones. It uses the least square method on the spectral lineouts in order to determine the optimal parameters providing the best fitting of the spectra. However, this method did not provide sufficient results, so a possibility to select the best spectra manually was included.

The user guide to COMPSPECT is attached in the appendix C, the screenshot of the code is in Fig. 6.1.

6. Sample application in experimental spectra evaluation

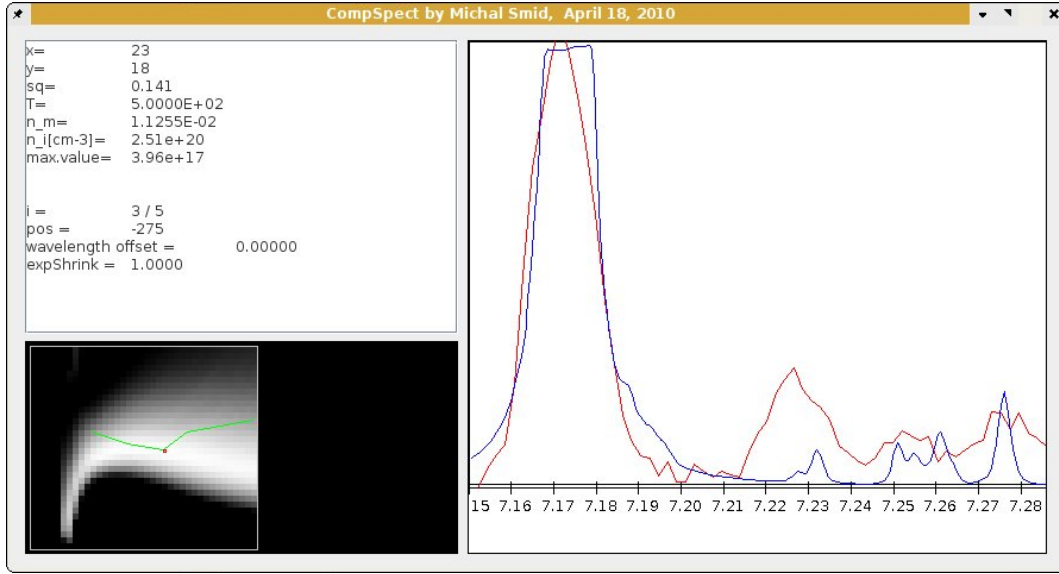


Figure 6.1.: Screenshot of the CompSpect application.

6.2. Experimental data

The sample experimental data to be evaluated are shown in Fig. 6.2. They are identical with those used for the spectra evaluation done in my research project. This data selection provides a possibility of comparing results of both approaches.

The target in this experiment consisted of 0.8 μm thick aluminium foil and 2 μm thick magnesium foil, with spacing 550 μm . The laser beam impinged the Al foil with energy $E = 193$ J and wavelength 1.315 μm .

In the lower part of Fig. 6.2, we can see the spectra emitted from the Al foil (positioned at the distance of 0 μm), and those close to the Mg foil viewed on the top (~ 550 μm). The outer couple of intensive lines corresponds to the resonant Al Ly_α line, the less intensive inner couple on the Al foil to the Al Ly_α J-satellite (~ 7.275 \AA). The horizontal line with no radiation at ~ 0 μm is the shade made by the unperturbed part of the Al foil. We can see the emission of the full group of the satellite lines from the Al foil spreading and damping on both its sides, and their intensification at ~ -200 μm , where they are also mixed with the Mg_δ (~ 7.31 \AA) and Mg_ϵ (~ 7.22 \AA) lines due to the collision of the counter-streaming plasma jets. Consequently, there is a density buildup in this region. The Al emission structure almost disappears at ~ 400 μm . Distinct Mg lines as well as the Al J-satellite and the resonance line can be seen on the Mg foil (~ 550 μm).

6. Sample application in experimental spectra evaluation

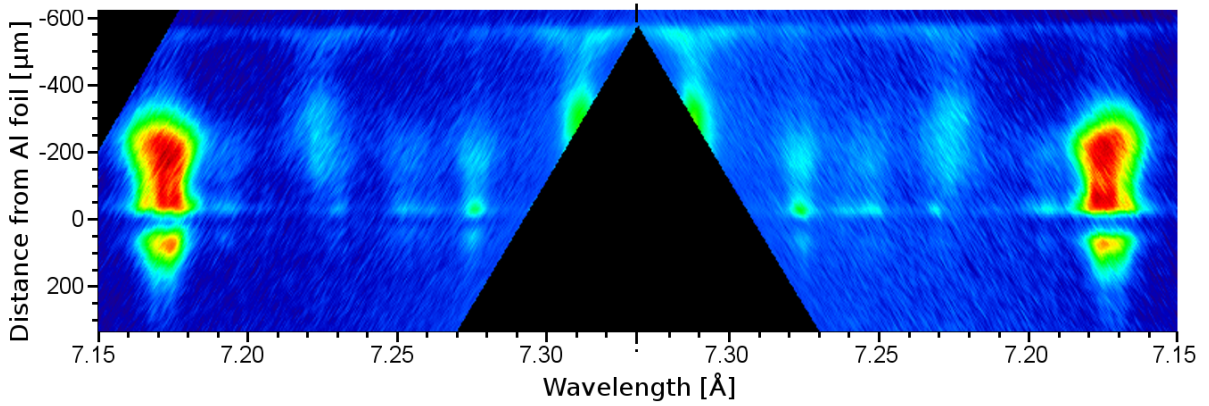


Figure 6.2.: Experimental spectra from the double-foil experiment selected for the evaluation. Al foil is positioned at $z = 0 \mu\text{m}$, Mg foil at $z = -550 \mu\text{m}$.

6.3. Single-cell evaluation

The single-cell evaluation of the experimental data performed using PRISM SPECT in year 2010 is briefly presented here. It approximated the plasma profile with $100 \mu\text{m}$ thick homogeneous plasma. In Fig. 6.3, there are five selected distinctive spectra from the measured range of the described experiment, fitted with simulated profiles with plasma parameters summarized in Tab. 6.1.

The spectra for $z = 555 \mu\text{m}$ and $344 \mu\text{m}$ are fitted with Mg simulation, while the other ones with Al. The midplane spectrum ($z = 190 \mu\text{m}$) was not fitted because no single-cell simulation was relevant. A typical plasma diluting with increasing distance from both foils can be seen.

6. Sample application in experimental spectra evaluation

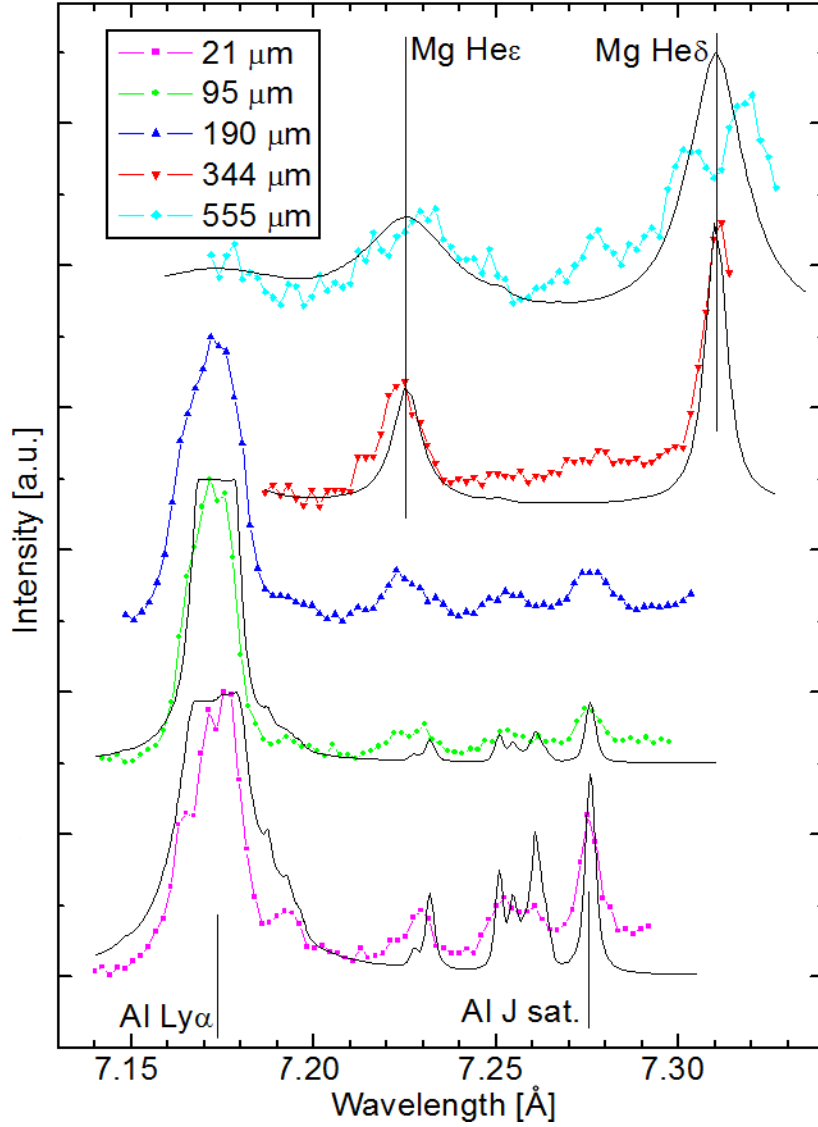


Figure 6.3.: Experimental data (points) fitted using the single-cell simulations (lines) for various positions between the foils.

distance [μm]	Material	T [eV]	n_i [cm^{-3}]
21	Al	300	4×10^{20}
95	Al	480	2×10^{20}
344	Mg	200	1×10^{20}
555	Mg	200	4×10^{20}

Table 6.1.: Parameters of single-cell PrismSpect simulations fitting of experimental data.

6.4. Results

The figure Fig. 6.4 shows the best fitting spectra from Cretin (black line) along the experimental data from $z = 95 \mu\text{m}$ (green points).

We can see a very good agreement between the synthetic and the experimental spectra, especially at the satellite lines with $\lambda > 7.18 \text{ \AA}$. Note that the experimental peak at $\approx 7.22 \text{ \AA}$ corresponds to the Mg He_c line which is not present in the Al simulation. The simulated resonance doublet line shows a deeper gap between the two peaks compared to the experimental one. This difference may be caused by smoothening of the experimental spectra due to the time-integration over the evolving plasma.

The plasma parameters profiles mapped to the simulation are depicted in Fig. 6.5 in solid lines, compared to the symbolical representation of the single-cell simulation parameters using dashed lines.

Compared to the previous results with the single-cell simulation in Fig. 6.3 (green), the overall agreement is substantially better showing the relevance of used methods, and is very promising for further research.

6. Sample application in experimental spectra evaluation

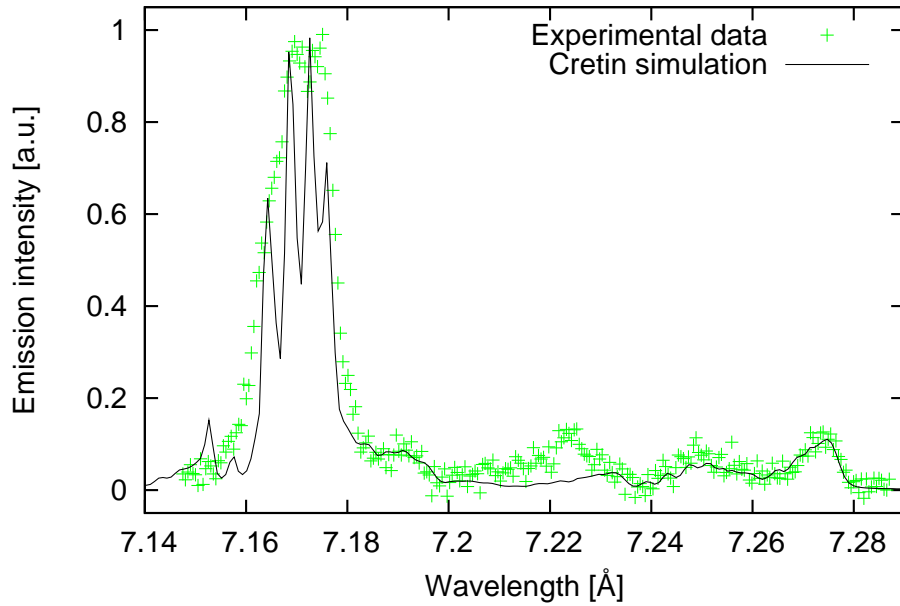


Figure 6.4.: Fitted synthetic spectra from *Cretin* (black) on the experimental data (green).

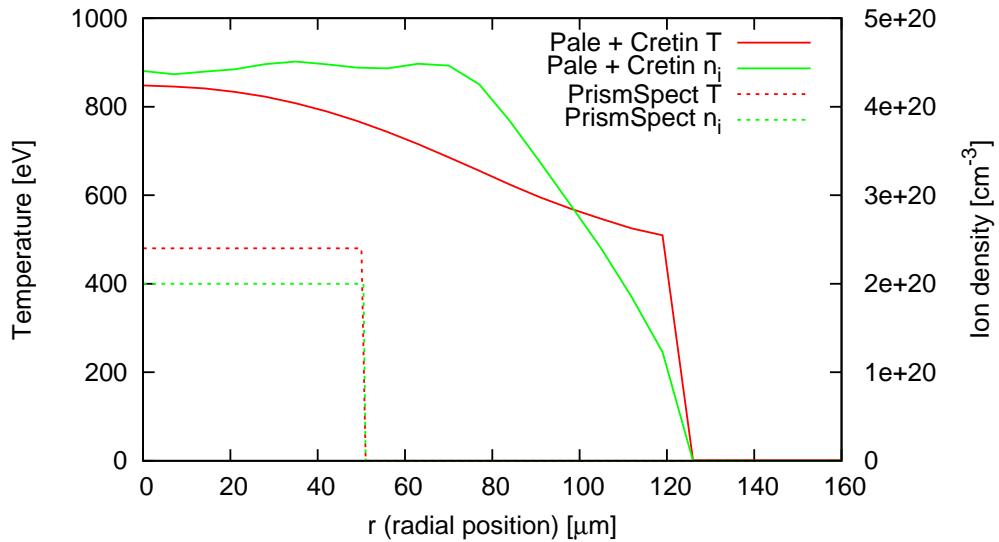


Figure 6.5.: PALE-simulated radial profile of plasma parameters after the fitting procedure using *Cretin* (solid lines), and the parameters of the single-cell 100 μm thick plasma of previous *PrismSpect* fit (dashed lines).

7. Conclusion

The strategic goal of this work was to contribute to the investigation of phenomena accompanying the interaction of laser-produced plasmas with secondary targets. Among diverse diagnostic methods applied in experiments performed at the Prague laser system PALS, the role of high-resolution x-ray spectroscopy is of paramount importance, being capable of providing information on environmental conditions in strongly coupled plasmas inaccessible for other diagnostics. My contribution to this research consists in participation in relevant PALS experiments and in interpretation of self-emission x-ray spectra characterizing the distribution of macroscopic plasma characteristics (in particular, temperature and density).

The main tasks of my thesis refer to the development of the computational framework dedicated to the evaluation of large-volume spectroscopic data. This effort is closely linked to my previous activities directed at the computational reconstruction of the experimental x-ray spectra (bachelor thesis *Spectroscopic investigation of laser-produced plasma interaction with solid targets*) and their simple theoretical interpretation (research project *Evaluation of emission x-ray spectra characterizing interaction of laser plasma with solids*). These activities were substantially extended by a successful implementation of diverse atomic and collisional-radiative codes, and their coupling to the hydrodynamics simulations performed by the PALE code.

The main results obtained within the frame of this thesis include:

- Creation of suitable atomic model using HULLAC and its implementation into CRETIN.
- Communication with H. Scott and M. Busquet on modifications and enhancement of their codes.
- Active participation in the PALS LPWI experiments, and reconstruction of high-resolution VJS spectra.
- Interconnection of CRETIN and PALE to postprocess the hydrodynamic data.

7. Conclusion

- Testing of various regimes of postprocessing using single-foil hydrodata.
- Sample usage of Cretin with PALE-derived gradients to evaluate measured spectra.
- Participation in several presentations / publications.[15][16][17][18]

The anticipated future work will be directed at:

- Usage of the developed tools (based on Cretin or PrismSpect codes) for evaluation of precisely measured x-ray spectra.
- Spectral postprocessing based on PALE simulations enhanced by the MULTIF code treatment which allows the modeling of colliding plasmas.
- Application of the developed framework to different plasma experiments directed at investigation of phenomena accompanying LPWI, plasma compression in jets, hot electron generation, transfer and propagation in different media, and charge exchange phenomena in field ionized plasma.

Bibliography

- [1] R.Liska, J.Limpouch, M.Kuchařík, O.Renner. Selected laser plasma simulations by ALE method. *Journal of Physics: Conference Series* 112 (2008) 022009 (1-4).
- [2] D. Salzmann. *Atomic Physics in Hot Plasmas*. Oxford University Press, 1998.
- [3] A. Cejnarova, L. Juha, B.Kralikova, J. Krasa, E.Krousky, P.Krupickova, L.Laska, K.Masek, T.Mocek, M.Pfeifer, A. Präg, O.Renner, K.Rohlana, B.Rus, J.Skala, P.Straka, J.Ullschmied, and K. Jungwirth. The Prague Asterix laser system. *Phys. Plasmas*, 8:2495, 2001.
- [4] O. Renner, T. Missalla, P. Sondhauss, E. Krouský, E. Förster, C. Chenais-Popovics, and O. Rancu. High-luminosity, high-resolution, x-ray spectroscopy of laser-produced plasma by vertical-geometry johann spectrometer. *Rev. Sci. Instrum.*, 68 (6):2393, June 1999.
- [5] O. Renner. *Pokročilá rentgenová spektroskopie vysokoteplotního hustého plazmatu*. DrSc thesis, Institute of Physics, AS CR, Prague, 1998.
- [6] M.Šmíd. *Spectroscopic Investigation of Laser-Produced Plasma Interaction with Solid Targets*. Bachelor thesis, Faculty of Nuclear Sciences and Physical Engineering, Czech Technical University, 2009.
- [7] F.B. Rosmej. *X-ray emission spectroscopy and diagnostics of non-equilibrium fusion and laser produced plasmas*, in R.Hutton (Ed.), *Highly Charged Ions*, Taylor and Francis, to be published 2011, ISBN 9781420079043.
- [8] H.R. Griem. *Principles of Plasma Spectroscopy*. Cambridge University Press, 1997.
- [9] H.-K.Chung, M.H.Chen, W.L.Morgan, Y.Ralchenko, and R.W.Lee. FLYCHK: Generalized population kinetics and spectral model for rapid spectroscopic analysis for all elements. *High Energy Density Physics*, 1:3, 2005.
- [10] J.J.MacFarlane, I.E.Golovkin, P.Wang, P.R.Woodruff, and N.A.Pereyra. SPECT3D-A Multi-Dimensional Collisional-Radiative Code for Generating Diagnostic Signatures

Bibliography

- Based on Hydrodynamics and PIC Simulation Output *High Energy Density Physics*, 3:181, 2007.
- [11] H.A.Scott. Cretin—a radiative transfer capability for laboratory plasmas. *Journal of Quantitative Spectroscopy and Radiative Transfer*, 71(2-6):689–701, 2001.
- [12] M.Busquet. Improved analytic fits of collisional cross-sections *High Energy Density Physics*, 3:48–51, 2007.
- [13] S.J. Goett, R.E.H. Clark, D.H. Sampson. *Atomic Data and Nuclear Data Table*, 25:185, 1980.
- [14] J.S.Wark, A.Djaoui, S.J.Rose, H.He, O.Renner, T.Missalla, and E.Förster. Effect of velocity gradients on x-ray line transfer in laser-produced plasmas. *Physical Review Letters*, 72:1826–1829, 1994.
- [15] O.Renner, E.Krouský, R.Liska, M.Šmíd, O.Larroche, E.Dalimier, and F.B.Rosmej. Direct spectroscopic observation of ion deceleration accompanying laser plasma-wall interaction *Journal of Physics: Conference Series*, 244 (2010) 022024.
- [16] O. Renner, J.Cihelka, L.Juha, E.Krouský, J.Nejdl, J.Skála, A.Velyhan, T.Pisarczyk, T.Chodukowski, P.Pisarczyk, R.Liska, M.Šmíd, P.Váchal, J.Velechovský, J.Ullschmied, O.Larroche, E.Dalimier. Spectroscopic Diagnosis of Energetic Plasma Jets Interaction with Walls, *14th International Workshop on Radiative Properties of Hot Dense Matter, Marbella*, October 4-8, 2010 (oral). Politecnica Madrid, Book of abstracts, p.20.
- [17] O. Renner, E. Krousky, R. Liska, M. Smid, O. Larroche, E. Dalimier. Ion collisions and deceleration in laser-produced plasma-jet interaction with walls, *25th Symposium on Plasma Physics and Technology*, Prague, June 14-17, 2010 (oral). Submitted to Topical issue Acta Technica (in print)
- [18] O.Renner, J.Cihelka, L.Juha, J.Krása, E.Krouský, J.Nejdl, J.Skála, A.Velyhan, T.Pisarczyk, T.Chodukowski, Z.Kalinowska, A.Kasperczuk, P.Pisarczyk, R.Liska, M.Šmíd, P. Váchal, J.Velechovský, J.Ullschmied. Plasma Jets Production at Laser-Burnt-Through Foils and their Interaction with Secondary Targets *5th Conference on Frontiers of Plasma Physics and Technology*, Singapore April 18-22, 2011, Singapore (oral). Submitted to IAEA Proceedings.

A. Hullac input files

There are four separate files necessary to generate the described atomic model using HULLAC, each one for one ionization state of aluminium.

Listing A.1: Lithium-like atoms

```
comment = 'Al-Li'
atom Al

SETTING
PATH='Al_Li'
END SET

DATA
potential NEW
GROUP Li
a 1s2 2s1
b 1s1 2s1 2p1
c 1s1 2p1 3p1
d 1s1 2p1 3s1
e 1s1 2p2
f 1s1 2p1 3d1
g 1s1 2p1 4p1
h 1s1 3d1 4p1

group Hegnd
1s2- 1s2
END DATA

PROCESS
energy all
excit all
ga Li
auto all
ioniz all
END process
ENDJOB
```

Listing A.2: Hydrogen-like atoms

```
comment = 'Al-H'
atom Al

SETTING
PATH='Al_H_'
END SET

DATA
potential NEW
GROUP H
1s 1s 1
2s 2s 1
2p 2p 1
3s 3s 1
3p 3p 1
3d 3d 1
4s 4s 1
4p 4p 1

GROUP nuc
bare
END DATA

PROCESS
energy all
excit all
ga H
auto all
ioniz all
END process
ENDJOB
```

A. Hullac input files

Listing A.3: Helium-like atoms

```
comment = 'Al He-like '  
atom Al  
  
SETTING  
PATH='Al_He_ '  
END SET  
  
DATA  
potential NEW  
group Hgnd  
1s 1s1  
potential NEW  
GROUP He  
1s2- 1s 2  
1s2p 1s1 2p1  
1s2s 1s1 2s1  
1s3s 1s1 3s1  
1s3p 1s1 3p1  
1s3d 1s1 3d1  
1s4s 1s1 4s1  
1s4p 1s1 4p1  
1s4d 1s1 4d1  
1s4f 1s1 4f1  
potential NEW  
2p2 2p2  
2s2p 2s1 2p1  
2s3p 2s1 3p1  
2s3d 2s1 3d1  
2p3s 2p1 3s1  
2p3p 2p1 3p1  
2p3d 2p1 3d1  
2p4d 2p1 4d1  
2p4s 2p1 4s1  
2p4p 2p1 4p1  
2s2 2s2  
potential NEW  
3d4p 3d1 4p1  
3d4s 3d1 4s1  
3p4d 3p1 4d1  
3p4p 3p1 4p1  
3p4s 3p1 4s1  
3p2 3p2  
3s2 3s2  
3s3d 3s1 3d1  
3s3p 3s1 3p1  
3s4s 3s1 4s1  
3s4p 3s1 4p1  
3s4d 3s1 4d1  
3d2 3d2  
3p3d 3p1 3d1  
END DATA
```

```
PROCESS  
energy all  
excit all  
ga He  
auto all  
ioniz all  
END process  
ENDJOB
```

Listing A.4: Beryllium-like atoms

```
comment = 'Al-Be '  
atom Al  
  
SETTING  
PATH='Al_Be_ '  
END SET  
  
DATA  
potential NEW  
GROUP Be  
A 1s2 2s2  
  
group Lignd  
a 1s2 2s1  
END DATA  
  
PROCESS  
energy all  
excit all  
ga Be  
auto all  
ioniz all  
END process  
ENDJOB
```

B. Generator files for Cretin

The input files for CRETIN defining the simulational parameters are included here. The Listing B.1 shows the file for single-profile simulations used in Case A or in experimental evaluation, Listing B.2 shows the generator file for simulations *C* and *D*, shortened in the detector definition.

Listing B.1: Cretin generator file for single profile simulation

```
c ----- Materials
atoms iz=13 Al_atomT.dat al
reg 1

c ----- Geometry
geometry slab
xfile current.xf
source ni 1 13 13 0 1.

c ----- Radiation
angles 2
c linedefault total
line 1 13 1 1 1 3
  linetype crd doppler
lbins 25 3. 1.02

line 2 13 1 1 1 4
  linetype crd doppler
lbins 25 3. 1.02

joinline 1 2

ebins 20 1690. 1750.
spectrum 300 1690 1750. 1.

c ----- Controls
restart
sdump

switch 11 1 ! make .plt file
switch 23 0 ! use isotropic scattering
switch 25 0 !Steady state (0) or Time-dependent(1)
switch 28 1 !Initialization LTE(0), CR steady st.(1)
switch 29 0 ! use xfile times
switch 30 10 ! dump every n timesteps
switch 33 4 ! use generalized escape factors
switch 36 0 ! no continuum transfer
```

B. Generator files for Cretin

```
switch 37 1      ! do line transfer
switch 38 1      ! symmetric line profiles
switch 52 -1     ! do Stark broadening for everything
switch 55 1      ! do continuum lowering
switch 72 10     ! do spectral calc.every n timesteps

switch 117 1     !Do not ignore warning messages from TOTAL

c ----- Edits
dump all history

editray 1 1.5 0. 0

plot "SPECTRUM"
  xvar  sp_wvl      0
  yvar  isp-        0 1 0 1
```

Listing B.2: Cretin generator file for complex simulations.

```
c ----- Materials
atoms iz=13 Al_atom.dat al
reg 1
c ----- Geometry

geometry rz
xfile lag.xf
source ni 1 13 13 0 1.

c ----- Radiation
angles 4 4
ebins 200 1690. 1750.
spectrum 400 1690 1750. 1.

c ----- Controls
restart
sdump

switch 11 1      !make .plt file
switch 23 0      !use isotropic scattering
switch 25 1      !Steady state (0) or Time-dependent(1)
switch 28 1      !Initialization LTE(0), CR steady-state(1)
switch 29 0      !use xfile times
switch 30 1      !dump every n timesteps
switch 33 4      !use generalized escape factors
switch 36 0      !no continuum transfer
switch 37 1      !do line transfer
switch 38 1      !symmetric line profiles
switch 52 -1     !do Stark broadening for everything
switch 55 1      !do continuum lowering
switch 72 1      !do spectral calculation every n timesteps
```

B. Generator files for Cretin

```
switch 8 0 !Scott's suggestion
switch 117 1 !Don't ignore warning messages from TOTAL

c ----- Edits
dump all history

alias PIH 1.5707
alias MU0 .001
alias RDet 1000e-4
c          det#          R      Z
detector  1          RDet -1.50e-02 MU0 PIH  0.01
detector  2          RDet -1.47e-02 MU0 PIH  0.01
detector  3          RDet -1.45e-02 MU0 PIH  0.01
detector  4          RDet -1.42e-02 MU0 PIH  0.01
...

plot "SPECTRUM"
  xvar  sp_wvl      0

yvar  spdetect 0    1
yvar  spdetect 0    2
yvar  spdetect 0    3
yvar  spdetect 0    4
...
```

C. CompSpect manual

C.1. Introduction

The COMPSPECT application helps to find the best fit between synthetic and experimental spectra. It uses the simulated spectra generated by e.g. the PRISMSPECT code, and experimental data eg. from the VJS ANALYSER application[6].

The fitting procedure is described in section C.3 , before using the application, it is recommended to read the general description in section C.2.

C.2. Application description

C.2.1. Configuration

The application requires a plain text configuration file COMPSPECT.CONF in the application directory, which is automatically loaded on program startup and can be reloaded using R key. Each row represents one parameter assignment. Rows beginning with the number sign (#) and empty rows are ignored. The configuration parameters are listed in Tab. C.1.

C.2.2. Simulated spectra input

The required structure of the simulated spectra is designed to be compatible with the output of the PRISMSPECT code.

The files in the given directory are organized according to their temperature and density into a 2D set, furthermore called GRID. They are called SPECT_XXXX_YYYY.PPD, where XXXX and YYYY stands for the coordinates within the grid. In the header of these files lines like

```
# Plasma temperature (eV)      = 8.0000E+02
# Mass density (g/cm3)         = 7.4466E-01
```

are searched and the plasma parameters of the spectrum are determined by them. The core of the file is a table, with two first columns: PHOTON ENERGY [eV]; EMISSION INTENSITY. Other columns are ignored.

C.2.3. Experimental spectra input

The required experimental spectra file structure is designed to be compatible with the output of the VJS ANALYSER. The spectra are written in plain text tables with two columns: PHOTON WAVELENGTH [Å]; EMISSION INTENSITY.

C. CompSpect manual

Parameter	Unit	Description
averageIonWeight	[g]	Average atomic weight, used to calculate the ion density ($n_i = \rho/\text{averageIonWeight}$)
expDir	[dir]	Directory containing experimental data
expShrink	1 [-]	Default factor correcting the wavelength axis of experimental data.
minl, maxl	[Å]	Minimal and maximal wavelength to be drawn in the plot.
fitMinl, fitMaxl	[Å]	Minimal and maximal wavelength to be fitted.
gridDir	[dir]	Directory containing results of the simulations.
gridDrawD	10 [px]	"Zoom" of the chart in N-T PANE .
subtractLinearOffset	[true/false]	If set to true, the linear background of each loaded experimental data will be estimated and subtracted.
subtractConstantOffset	[true/false]	If set to true, the constant background of each loaded experimental data will be estimated and subtracted. The value can be manually set even if this option is set to FALSE.

Table C.1.: Application parameters.

For processing the set of spatially resolved spectra, the files need to be called LXXX.DAT, or RXXX.DAT, where XXX stands for the spatial coordinate assigned to this spectrum.

C.2.4. Experimental spectra adjustment

Each experimental spectrum undergoes following corrections before being fitted:

1. The wavelength axis is corrected using formula $\lambda_{\text{new}} = \lambda_{\text{min}} + \text{expShrink} * (\lambda_{\text{old}} - \lambda_{\text{min}})$
2. The linear, resp. constant intensity background is determined and subtracted, if the SUBTRACTLINEAROFFSET, resp. SUBTRACTBACKGROUNDOFFSET is set to true.
3. The spectrum intensity is normalized to $I_{\text{max}} = 1$.
4. The wavelength axis is shifted using formula $\lambda_{\text{new}} = \lambda_{\text{old}} + \text{offset}$, where OFFSET is automatically determined during the fitting process.

C.2.5. Automatic spectra fit

The best fit of a spectrum is determined as the one with the least sum of squares of differences between the experimental and the simulated intensities. During the automatic process, also the best wavelength offset is determined.

C.2.6. Application window

The application window consists of three panes: The largest SPECTRA PANE on the right-hand side shows the spectra (in the linear intensity scale), the MESSAGE PANE in the upper left corner shows textual information from the application, and the N-T PANE in the bottom left corner shows the density – temperature chart to help with the navigation through the simulated spectra.

C.2.7. n-T pane

The N-T PANE contains a chart, where the horizontal axis corresponds to the temperature, increasing to the right and the vertical axis corresponds to the density, increasing to the bottom.

The position of the red pointer is given by the parameters of the actual simulated spectrum. The green line depicts the result of experimental spectra evaluation: Each point is related to one loaded experimental spectrum, and its position is given by the parameters of the assigned simulated spectrum. The points are connected into the line based on the spatial order of the experimental spectra.

The darkness of the background of the chart in a given point indicates the difference between the simulated spectrum corresponding to the point and the current experimental one.

C.2.8. Output files

The output files characterize the plasma parameters in dependence on the spatial position of the spectra emission.

The files are text tables with first column SPATIAL POSITION [μm] and the second one the PLASMA TEMPERATURE [eV] in the TEPMERATUREX file, or the PLASMA DENSITY [g/cm^3] in the DENSITYX file, where X stands for L, resp. R for the left-hand side, resp. right-hand side spectra.

C.3. Usage guide

C.3.1. Fitting the set of spectra - creating the temperature / density profiles

1. Set all necessary parameters within the configuration file, start the application.
2. press E, the dialog appears to confirm or change the GRIDDIR directory, and the simulation data will be loaded from there.
3. press F, resp. G, the dialog appears to confirm or change the EXPDIR directory, and the left-hand side, resp. right-hand side experimental spectra from this directory will be loaded and automatically fitted with the simulated ones.

4. Go through the experimental data using the PgUp/PgDown keys and correct the "best fit" for each experimental spectrum using the arrows. Confirm the n, T assignment for the given spectrum using I key.
5. Press K, the output files will be saved into the EXPDIR directory.

C.3.2. Manual assignment of the corresponding spectrum

This section gives a more detailed description of step 4 in section C.3.1.

The PgUp / PgDown keys navigates through the experimental spectra. The selected spectrum is drawn in the SPECTRA PANE in red color, the corresponding simulated one in blue color. The parameters of both spectra are written in the MESSAGE PANE, as described in the following table.

Parameter	Meaning
Current simulated spectrum parameters	
x, y	Coordinates within the GRID, given by the spectrum file-name.
sq	Sum of squares of differences between the current simulated and experimental spectrum.
T	Plasma temperature [eV].
n_m	Mass density [g/cm ³].
n_i	Ion density [ions/cm ³], calculated as $n_i = \rho / \text{averageIonWeight}$.
max.value	Maximum intensity.
Current experimental spectrum parameters	
i	Index within the set of spectra.
pos	Spatial position[μm].
offset	Wavelength offset, determined during the fitting process.
expShrink	Actual value of EXP SHRINK parameter.

For each experimental spectrum, the user can navigate within the GRID using the arrow keys. The intensity of subtracted constant background, and the normalization factor can be manually interactively set using the (SHIFT +) A/Z keys.

After the best simulated spectrum is selected, press the I key to confirm.

C.3.3. Fitting of one spectrum

1. press E, simulation data will be loaded.
2. press W and a file open dialog will appear to select and load the experimental spectrum.
3. press B, the fit will be performed and its result will be shown in the SPECTRA PANE.

C.3.4. Average profile function

This function takes two files containing two-column tables, assumes the first column in both tables are identical, and generates an output file, where the first column is identical to the input files, and the second column is the average of the input files second columns.

It is especially useful for creating the average temperature or density profiles from the ones generated from the left-hand and right-hand side spectra. To use it press the L key, select the two files to be averaged using the dialog and set the name for the result in the flowing dialog.

C.3.5. Convert energy axis function

This function can be used either for simple conversion of spectra between energy and wavelength scale, or to replace the energy scale of one spectrum with a scale from another spectrum, interpolating the intensity values.

For simple conversion, press C, select whether the source file x-axis is in [eV] or [\AA], select the file, do this once again and then select the output file.

For replacing the x-axis (either energy or wavelength), press C, select the file containing desired x-axis values, then select the spectrum to be converted, finally select the output file.

The result is a spectrum, where the x-axis values are copied from the first loaded file, while the intensity values are taken from the second file and interpolated to the current x-axis values.

C.4. Keystroke function reference

All functions are accessed via single keystrokes summarized in the following table.

C. *CompSpect* manual

Key	Function
R	Reloads configuration file.
E	Loads simulated data.
W	Asks for a single experimental spectrum file and loads it.
F,G	Asks for a directory containing set of spectra files and loads the left-hand side, resp. right-hand side ones.
Q	Replots spectra. (Use if they are not properly shown.)
B	Fits the experimental data on the loaded grid.
I	Sets current simulated spectrum as the best one.
K	Saves current temperature and gradient profile to file.
A,Z	Increases resp. decreases the subtracted background of experimental data.
Shift+A, Shift+Z	Increases resp. decreases the normalization coefficient.
F, G	Loads and fits whole set of left-handed, respectively right-handed experimental data.
arrows	Navigates through the simulated spectra.
PgUp/ PgDown	Navigates through the loaded experimental data.
L	Average two profile data files.
C	Convert energy axis function.